Research Square

Preprints are preliminary reports that have not undergone peer review.
They should not be considered conclusive, used to inform clinical practice,
or referenced by the media as validated information.

The silhouette of a vibrated sessile drop encodes its internal viscous dissipation

Ahmad Naseri Karimvand
University of Tennessee at Knoxville
Daren Watson
Florida Polytechnic University
Andrew Dickerson
ad@utk.edu

University of Tennessee at Knoxville https://orcid.org/0000-0003-1220-1048

Research Article

Keywords: cantilever, internal flow, sloshiness, sessile drops, viscosity

Posted Date: September 11th, 2026

DOI: https://doi.org/10.21203/rs.3.rs-10998220/v1

License: This work is licensed under a Creative Commons Attribution 4.0 International License.
Read Full License

Additional Declarations: The authors declare no competing interests.

The silhouette of a vibrated sessile drop encodes its internal viscous dissipation

Ahmad Naseri Karimvand[a], Daren A. Watson[b], & Andrew K. Dickerson[a,*]

[a]Department of Mechanical and Aerospace Engineering, University of Tennessee
Knoxville, TN, 37996, USA

[b]Department of Mechanical Engineering, Florida Polytechnic University,
Lakeland, FL, 33805, USA

[*]Corresponding author: ad@utk.edu

September 10, 2026

Abstract

Viscous dissipation in a deforming drop is a result of internal velocity gradients, and so direct measurement has therefore required optical or computational access to the drop interior. For sessile drops undergoing predominantly single-mode oscillations, we show that the volumetric viscous dissipation rate is proportional to the time rate of change of a scalar measure of silhouette deformation. The dissipation rate per unit volume is proportional to the dynamic viscosity and the square of the rate of change of the drop silhouette deformation. We obtain this result by decomposing the silhouette deformation into data-driven modes and reconstructing the associated interior strain-rate field. We validate our theoretical approach against measured ring-down dissipation over a 33-fold range of viscosity. For a steady, oscillatory forcing, an energy balance combined with a base-excited oscillator analogy and a Stokes boundary-layer correction predicts the power transmitted from a vibrating substrate. The model reproduces measurements for a withheld fluid in the drop pre-resonance regime. We identify the ratio of Stokes penetration depth to drop height as the parameter governing volumetric energy transfer from the vertically oscillating substrate into the drop, and predict that transfer is non-monotonic in both viscosity and drop size. A thin shear layer engages too little of the drop, while a layer spanning the drop height homogenizes the velocity field and suppresses shear. Cantilever ring-down experiments confirm our predictions. Our measurement approach, which requires only the drop silhouette, estimates the bulk dissipation that inviscid sessile-drop theory structurally omits in systems where the interior is optically or practically inaccessible.

Keywords: [cantilever, internal flow, sloshiness, sessile drops, viscosity]

1 Introduction

Drop dynamics are governed by inertia [1,2], capillarity [3], viscosity [4], and wetting [5]. A sessile drop (**Fig. 1**a) on a vibrating surface behaves as a miniaturized resonator that temporarily stores and subsequently dissipates mechanical energy [6]. A fraction of the vibration energy from the underlying surface is transferred into the liquid bulk, generating internal flows and deformation of the liquid–gas interface [7,8]. This energy is partly and reversibly stored as surface energy through changes in interfacial area and partly dissipated by internal viscous stresses and contact-line friction at the three-phase boundary [9,10].

Understanding how vibration energy is transmitted to a drop and how that energy is dissipated is pertinent to a broad range of physical systems, which we organize into three categories. First, dissipation measurements underpin several fundamental characterization techniques. In oscillatory rheology, Lissajous curves representing the energy dissipated per deformation cycle are used to measure the rheological properties of complex liquids [11], and the damping rate of an oscillating drop can be used to determine the dynamic viscosity, surface tension, and rheological properties of the liquid [12]. Second, accurate estimation of viscous dissipation due to internal friction [13] is critical to predict the physics behind drop-impact outcomes, such as deposition, partial rebound, rebound, jetting, and splashing [14]. For example, with respect to a drop impacting a non-compliant surface, an improved viscous energy estimation significantly reduces inaccuracies when numerically predicting the maximum spreading diameter of the drop [15]. Third, dissipation plays

a key role in several engineering applications. Vibration-driven internal flows can excite non-axisymmetric modes and accelerate the mixing of biological reagents[16]; designing vibration-based decontamination systems for critical surfaces on robotic platforms requires characterizing the energy dissipated by sessile drops[17]; and the relationship between dissipation and resonant transitions can be used to control the transport and deposition morphology of colloidal particles during drop evaporation[18].

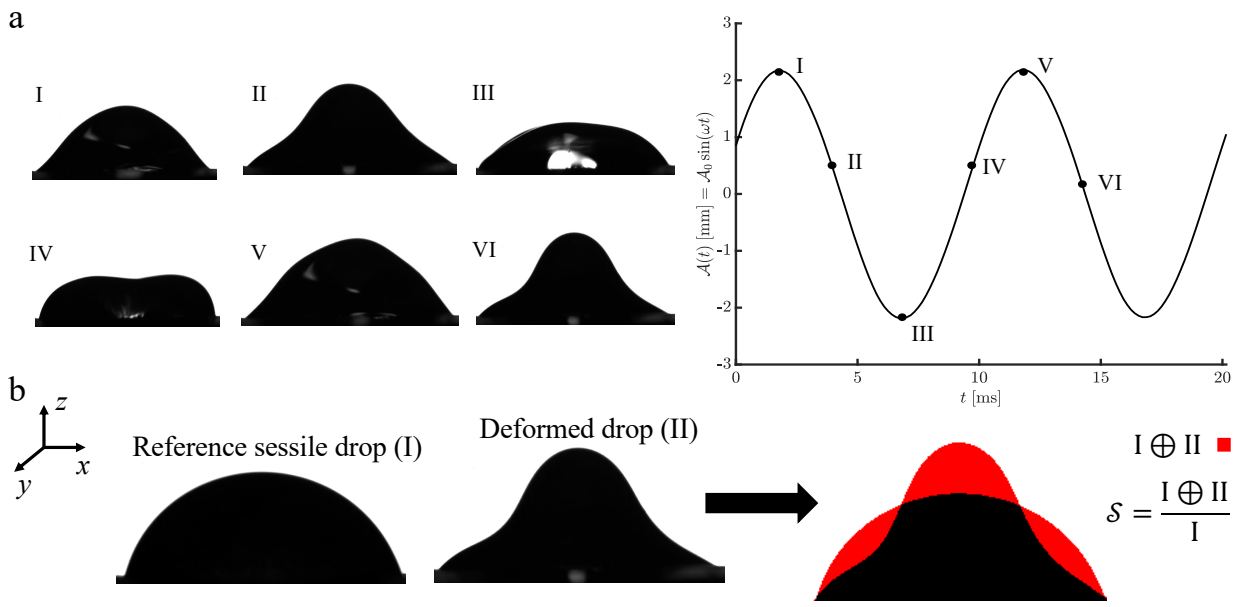


Figure 1: Drop silhouettes. **(a)** 5 μL drop on a vertically oscillating substrate with amplitude $\mathcal{A}_0$ and vibrating frequency ω. **(b)** Sloshiness ($\mathcal{S}$) as the exclusive difference ratio of a deformed drop relative to its sessile reference.

Despite the importance of quantifying energy dissipation in a drop, doing so remains difficult because the dependence on velocity gradients within the liquid[19,20]. We note that viscous dissipation represents the conversion of mechanical energy into heat at the scales over which velocity gradients vary, and such scales for oscillatory flows are set by the viscous penetration depth[20,21] $\delta_v = \sqrt{2\nu/\omega}$, where ν is the kinematic viscosity and ω is the angular frequency of oscillation. Conventional measurement techniques for resolving velocity gradients at length scales comparable to the size of a drop require high spatial resolution and expensive experimental setups[22,23]. Particle image velocimetry (PIV), whose accuracy depends strongly on the size of the interrogation window and the characteristic gradient length scale, is one of the most widely used experimental methods for estimating velocity fields[24]. Given that PIV provides a spatially filtered average of particle displacement, resolving velocity gradients accurately requires an interrogation window small compared to the length scale over which the flow varies[25]. Shrinking the window, however, also reduces the number of tracer particles it contains, degrading the reliability of the underlying correlation[25]. This trade-off is especially relevant for a drop, in which the relevant gradient length scale, the viscous penetration depth δ_v, can reach tens of micrometers, requiring interrogation windows of comparable size. Achieving even this resolution requires specialized micro-PIV instrumentation[26], whose measurement accuracy often benefits from ensemble averaging over multiple realizations of nominally identical flow fields[27,28], an approach that is not applicable to a single, non-repeating transient event. PIV's shortcomings are further exacerbated in a liquid drop by optical refraction and reflection at the curved interface, which distort the path of the laser light and misplace the velocity vectors[29]. Although ray-tracing corrections are applicable to stationary drops, they are impractical for oscillating drops whose surface contour changes continuously[30]. Additionally, Brownian motion of tracer particles in creeping flows often found within micro-scale drops is a significant source of measurement uncertainty[31].

Beyond velocity-field measurements, several alternative approaches have been used to estimate viscous dissipation, though most were developed for drop-impact problems rather than oscillating sessile drops. The analytical energy-balance method applies conservation of energy to predict post-impact behavior[32] while assuming that drops adopt a simple geometric shape at maximum spread[13,14]. In contrast, high-speed imaging and computational results show that real drop shapes and internal flows are considerably more complex[14]. Scaling-law analysis offers a complementary empirical perspective, but does not attempt to quantify the dissipated energy directly[14] and often breaks down for impact

velocities where dynamic wetting and contact angle effects, typically neglected in such models, become significant[33]. Weakly nonlinear theory uses perturbation expansions to solve for shape oscillations analytically, but its accuracy deteriorates once the deformation amplitude exceeds roughly 40% of the drop radius[12]. Computational methods can track individual energy terms in detail[34], but remain computationally expensive[15,34] and sensitive to the treatment of boundary conditions, particularly where the contact line is free to advance or recede across the solid surface rather than remaining pinned[33]. For oscillating sessile drops specifically, natural frequencies and mode shapes have been predicted by extending Rayleigh's classical free-drop spectrum[35] to account for substrate contact[36,37], with predictions confirmed experimentally via high-speed imaging[38]. The model developed by Bostwick & Steen (2014)[36] assumes an inviscid bulk fluid, so bulk viscous dissipation is necessarily zero throughout the analysis. A later viscous potential flow (VPF) correction[39] improves the frequency predictions but evaluates dissipation from an assumed curl-free velocity field rather than a true rotational, no-slip flow. Given these limitations, an approach that infers dissipation from the visible deformation of the drop is valuable for providing new insights into its energetics. Therefore, given the widespread use of high-speed videography for tracking drop shape, we seek to establish a quantitative connection between image-based silhouettes of drop deformation (**Fig. 1**b) and viscous dissipation measurements.

The image-based scalar, termed 'sloshiness' (S), is introduced in our study to quantify drop deformation from the instantaneous silhouette of a sessile drop relative to its equilibrium geometry (**Fig. 1**b).

Here, we connect the time rate of change of drop silohuette deformation to the volumetric viscous dissipation rate and the transmitted power for Newtonian drops formulated by a mixture of water and glycerol. In doing so, we demonstrate how the rich physics within a drop interior are encoded in the drop silhouette. Mixture ratios and drop properties are tabulated in Table 1. A base-excited spring-mass-damper analogy is employed to develop a semi-empirical model used to determine the relation between transmitted power and excitation frequency, substrate amplitude, liquid properties, and drop geometry. To experimentally test our model, plucked-cantilever experiments are used to measure energy transfer from the vibrating substrate to the drop, thus providing an experimental test of the use of image-based silhouettes to quantify energy dissipation and transmission during drop deformation. We present our experimental methods for substrate excitation, drop formulation, drop deformation, silhouette visualization, and plucked cantilever experiments in Section 2. Results and theoretical considerations are presented in Section 3, and the implications of this work discussed in Section 4. We conclude the study in Section 5.

2 Experimental methods

A schematic of our experimental setup is shown in **Fig. 2**. Drops are vibrated atop a 1.5×1.5-cm 1000-grit sandpaper mounted to a Modal Shop K2007E01 electrodynamic shaker that receives a 225 mV sine waveform signal from a Koolertone JDS6600–15 MHz digital signal generator, corresponding to a measured substrate displacement amplitude of 2.2 mm. Excitation frequencies range from 50 to 155 Hz with 15 Hz increments. For increased resolution near resonance, the frequency increment is reduced to 5 Hz in the vicinity of each drop natural frequency. Substrate temperature is monitored in real time using an Etekcity LaserGrip 1080 infrared thermometer and experiments are halted if this temperature deviates by more than ± 1°C from room temperature (23°C) to maintain experimental consistency across replicate trials.

Table 1: Physical properties of [W]ater and [G]lycerol mixtures used as sessile drops.

Mixtures	Mixture Ratio (water:glycerol)	Density, ρ (g/cm^3)	Dynamic Viscosity, μ (mPa·s)	Contact Angle, θ (°)
1W0G	1:0	1.00	0.88 ± 0.02	85.5 ± 0.8
3W1G	3:1	1.06	2.26 ± 0.54	79.0 ± 1.6
1W1G	1:1	1.13	6.48 ± 1.15	86.6 ± 2.2
1W3G	1:3	1.20	29.44 ± 2.02	84.8 ± 0.4
0W1G	0:1	1.26	393.50 ± 3.49	87.2 ± 1.8

Drops are formulated by mixing different proportions of water and glycerol. The reference dynamic viscosities of water and glycerol in our possession are $\mu = 0.88$ mPa·s and $\mu = 395.50$ mPa·s, respectively. Viscosity measurements

($N = 3$) for the formulated mixtures are obtained using a TA Instruments Discovery HR-20 rheometer in steady-shear mode, with a custom concentric cylindrical geometry, a bob diameter of 10.10 mm, and a cup diameter of 10.84 mm at room temperature. Equilibrium contact angles ($N = 3$) are measured photographically from the sessile drop method[40]. Here, three solutions are used, in addition to pure water (1W0G) and pure glycerol (0W1G): 3 parts water to 1 part glycerol (3W1G); 1 part water to 1 part glycerol (1W1G); and 1 part water to 3 parts glycerol (1W3G). Mixtures are tested in three sessile drop volumes: 3, 5, and 7 μL. The relevant properties of our drop mixtures are summarized in Table 1.

Sloshing experiments are recorded at 12,000 frames per second with two orthogonally positioned Photron NOVA S6 high-speed video cameras fitted with SIGMA 105-mm lenses. The experimental frame rate provides $77 - 240$ frames per oscillation cycle, corresponding to the tested range of excitation frequencies. Neewer NL-288A RC LED light panels are used to create drop silhouettes by backlighting experiments. Recorded videos are decomposed into individual images, which are then binarized in MATLAB with no imposed dilation or erosion. Each experimental condition has five replicates. To quantify drop kinematics, spatial measurements are smoothed using a Savitzky–Golay filter[41,42] to reduce high-frequency image-processing noise before numerical differentiation[40,43–45]. The chosen Savitzky–Golay filter performs local least-squares third-order polynomial smoothing within a 21-point moving window. Savitzky–Golay filters act as approximate low-pass filters whose cutoff frequency is jointly set by window length and polynomial order[42]. For these parameters and a frame rate of 12,000 fps, the resulting cutoff frequency is ≈ 795 Hz[46], approximately an order of magnitude above the $50 - 155$ Hz driving range and well below the Nyquist frequency. This separation ensures that the oscillatory signal is preserved while high-frequency image-processing noise is attenuated.

To corroborate the role of drop volume and viscosity in our semi-empirical model, we conduct experiments with a plucked free cantilever with length 28 mm and width 17 mm, following the methods of Alam *et al.* (2021)[17]. The cantilever, made with the same material as our vibrating substrate, is gently pushed downward by a plucker placed horizontally on a height-adjustable stage and time-dependent deflections captured once the cantilever releases from the plucker.

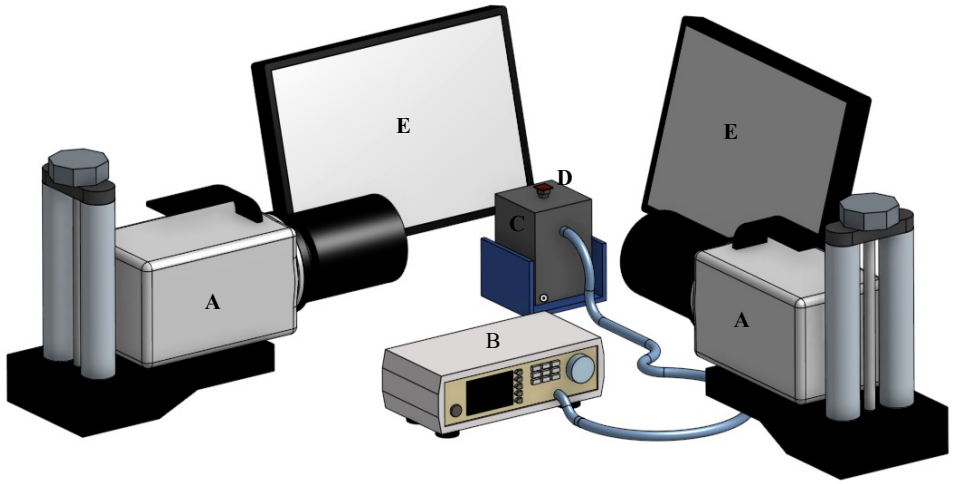


Figure 2: The schematic of the experimental setup used for capturing the deformation of the drop on an oscillating surface controlled by a signal generator. (A) orthogonally positioned Photron NOVA S6 high-speed video cameras fitted with SIGMA 105-mm lenses. (B) Koolertone JDS6600–15 MHz digital signal generator sending 225 mV sine waveform signal to (C) Modal Shop K2007E01 electrodynamic shaker on which (D) a 1.5×1.5-cm 1000-grit sandpaper is mounted. (E) Neewer NL-288A RC LED light panels are used to provide the backlighting creating contrast between the silhouette and the background.

3 Results

We present our experimental and modeling results in two steps. First, we consider how silhouettes can be employed to quantify viscous dissipation in drops undergoing ring-down from a perturbed state. Second, we consider a drop on a surface with sinusoidal vertical oscillation. We show how silhouettes can quantify the rate of energy transmission to

the drop, which, on average over a cycle, equals the dissipation rate. The model developed in this second step suggests that the ability of a drop to dissipate energy is non-monotonic with drop size and viscosity.

3.1 Sloshiness-rate-based quantification of drop energy dissipation

We represent the binarized images from two orthogonal camera views at time t as matrices $F_x(t)$ and $F_y(t)$, in which pixels inside the drop projection are assigned a value of one and all others are zero. The matrices at the initial frame, $F_x(0)$ and $F_y(0)$, correspond to the undeformed state of the drop. Each matrix $F_x(t)$ and $F_y(t)$ is registered such that its origin coincides with the midpoint of the two-dimensional contact line between the drop and the surface, at every time t. Therefore, sloshiness is defined as

$$S(t) = \frac{a^2 \sum_i \sum_j |F_x(t)_{i,j} - F_x(0)_{i,j}| + b^2 \sum_i \sum_j |F_y(t)_{i,j} - F_y(0)_{i,j}|}{a^2 \sum_i \sum_j F_x(0)_{i,j} + b^2 \sum_i \sum_j F_y(0)_{i,j}}, \tag{1}$$

where a and b are pixel-to-length conversion factors for each orthogonal view. Each element of the matrices F_x and F_y corresponds to an individual pixel, so sloshiness S is a dimensionless, image-based scalar that quantifies instantaneous drop deformation relative to its equilibrium sessile shape. While sloshiness is quantifiable with imaging, its connection to liquid properties is not yet established.

Sloshiness is defined directly from pixel data (Eq. (1)) and its simplicity is why it remains the quantity used throughout this work. Its connection to the underlying physics of dissipation, however, is not evident from its definition alone. We therefore turn to singular value decomposition (SVD), a data-driven modal decomposition, to establish this connection. SVD, equivalently proper orthogonal decomposition[47], has previously been applied to images of oscillating sessile drops to extract modal frequencies and to provide the first experimental validation of a spring-mass-damper analogy for the drop fundamental mode[48]. Here, we use this decomposition to derive the viscous dissipation rate directly in terms of the sloshiness rate $\dot{S}(t)$. For each video, the deformation field is assembled into a matrix $\boldsymbol{\chi} \in \mathbb{R}^{M \times N}$, where M is the number of tracked points on the drop contour and N is the number of video frames. Each column of $\boldsymbol{X}$ contains the displacement of all tracked surface points from the equilibrium sessile shape. The reference (equilibrium) positions of the points, measured from the drop centroid, are denoted $\mathbf{r}^{(0)} = \{r_k^{(0)}\}_{k=1}^{M}$. Applying SVD gives[49,50]

$$\boldsymbol{X} = \mathbf{U}\boldsymbol{\Psi}\mathbf{V}^T, \tag{2}$$

where $\mathbf{U} \in \mathbb{R}^{M \times P}$ and P is the number of modes present in the deformation. The pth column of $\mathbf{U}$, denoted $\mathbf{u}_p$, is a spatial mode whose entries indicate the relative displacement amplitude of each tracked point for that mode. Values near ± 1 correspond to maximal deformation, and values near zero indicate pinned (non-deforming) regions. Three representative cases—sessile, $+90°$ phase, and $-90°$ phase relative to the start of oscillation—are shown in **Fig. 3**. Point A is pinned, therefore, the corresponding element $\mathbf{u}_1$ would be 0. If point B is the most mobile point, its element would be ± 1, and point C has the opposite sign because when point B displaces in one direction, point C displaces in the opposite direction. $\boldsymbol{\Psi}$ is a diagonal matrix whose pth diagonal entry, σ_p, quantifies the strength of the corresponding mode $\mathbf{u}_p$. SVD modes are extracted empirically from image data and are not constructed to match any theoretically predicted spherical-harmonic mode shape, such as those classified by polar and azimuthal wavenumber $[k, \ell]$ (respectively the degree and order of the spherical harmonic) for sessile drops[36,38]. A given spatial mode $\mathbf{u}_p$ may therefore represent a single $[k, \ell]$ mode, a mixture of several, or neither. The single-mode approximation used below requires only that one such empirical pattern dominates, not that it be identified with any particular $[k, \ell]$ mode.

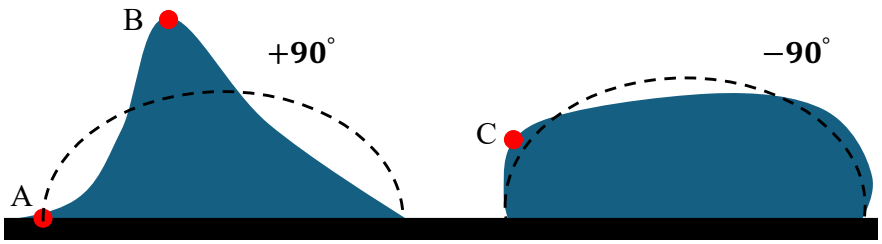


Figure 3: Schematic representation of sessile-drop deformation during vibration. The initial sessile drop shape is depicted by the dashed outline. Points A, B, and C indicate representative material points.

The columns of $\mathbf{V}$ (equivalently, the rows of $\mathbf{V}^T$) are temporal coefficient vectors $\mathbf{q}_p(t)$ that modulate the spatial modes frame by frame. The diagonal entries of $\mathbf{\Psi}$, ordered by mode, quantify the relative importance of each mode. A rapid decay of successive singular values indicates that few modes dominate the deformation. Assuming the deformation is dominated by the first SVD mode (i.e., $\sigma_1 \gg \sigma_2$), the deformation matrix can be approximated by,

$$\boldsymbol{X} \approx \mathbf{u}_1 \sigma_1 \, \mathbf{q}_1^T, \tag{3}$$

where $\mathbf{u}_1$ is the dominant spatial deformation pattern and $\mathbf{q}_1$ is its temporal coefficient vector. The optimality property of the singular value decomposition[51] guarantees that, among all possible rank-one approximations of $\boldsymbol{X}$, the truncation $\mathbf{u}_1\sigma_1\mathbf{q}_1^T$ minimizes the mean-square reconstruction error, $\|\boldsymbol{X} - \mathbf{u}_1\sigma_1\mathbf{q}_1^T\|_F^2 = \sum_{i\geq 2}\sigma_i^2$, in the sense of the energy norm[47] $\|\boldsymbol{X}\|_F^2 = \sum_{k,j} X_{kj}^2 = \sum_i \sigma_i^2$. This optimality means no other single spatial pattern could achieve a smaller reconstruction error than $\mathbf{u}_1\sigma_1\mathbf{q}_1^T$. In our experiments, the first mode captures around 75–80 % of the total energy ($\sigma_1^2/\sum_i \sigma_i^2$), supporting the single-mode approximation. Therefore, the deformation field at frame j can be written as

$$\chi(t_j) \approx \mathbf{u}_1 \sigma_1 \, q_1(t_j)\,, \tag{4}$$

where χ denotes the deformation, defined as the displacement from the equilibrium sessile shape. Using the definition of sloshiness in Eq. (1), the instantaneous deformation is normalized by the fixed equilibrium drop size $\sum_{k=1}^{M}|r_k^{(0)}|$,

$$\mathcal{S}(t) = \frac{\displaystyle\sum_{k=1}^{M}|\chi_k(t)|}{\displaystyle\sum_{k=1}^{M}|r_k^{(0)}|}. \tag{5}$$

Substituting Eq. (4) into Eq. (5) gives

$$\mathcal{S}(t) = \frac{\sigma_1\,|q_1(t)|\displaystyle\sum_{k=1}^{M}|u_{1k}|}{\displaystyle\sum_{k=1}^{M}|r_k^{(0)}|} = \beta\,|q_1(t)|, \qquad \beta = \frac{\sigma_1\displaystyle\sum_{k=1}^{M}|u_{1k}|}{\displaystyle\sum_{k=1}^{M}|r_k^{(0)}|}. \tag{6}$$

The corresponding reduced-order interior velocity field can be approximated as the time derivative of the displacement field,

$$w_i(\mathbf{x},t) = \frac{\partial \chi_i}{\partial t} = u_{1i}(\mathbf{x})\,\sigma_1\,\dot{q}_1(t)\,, \tag{7}$$

where w_i denotes the internal velocity field in the direction of i. Note that since $\mathbf{u}_1\sigma_1$ and the reference positions $\mathbf{r}^{(0)}$ are time-independent, the time derivative acts solely on $q_1(t)$. We construct $\mathbf{w}$ by extending the dominant surface mode into the drop volume, motivated by the classical result that, for low-order modes, interior flow is closely coupled to surface deformation[52,53]. Unlike the potential-flow construction used in these classical treatments, which guarantees a divergence-free field by solving Laplace's equation, our extension of $\mathbf{u}_1$ is not obtained this way and is not guaranteed to satisfy $\nabla\cdot\mathbf{w} = 0$ everywhere in the drop.

For a general Newtonian fluid, the viscous dissipation rate is[20]

$$\Phi(t) = \frac{1}{V}\int_V \left[2\mu\, D'_{ij}(\mathbf{x},t)\, D'_{ij}(\mathbf{x},t) + \kappa\,\Theta(\mathbf{x},t)^2\right]\mathrm{d}V, \tag{8}$$

where μ is the dynamic (shear) viscosity, κ is the bulk viscosity, V is the drop volume, and the strain-rate tensor (D_{ij}), its trace (the local dilatation rate) (Θ), and its deviatoric (trace-free) part (D'_{ij}) are[20,54,55]

$$D_{ij}(\mathbf{x},t) = \frac{1}{2}\left(\frac{\partial w_i}{\partial x_j} + \frac{\partial w_j}{\partial x_i}\right), \qquad \Theta(\mathbf{x},t) = D_{kk} = \nabla\cdot\mathbf{w}, \qquad D'_{ij} = D_{ij} - \frac{1}{3}\delta_{ij}\Theta. \tag{9}$$

The local dilatation rate Θ is expected to be negligible for two independent reasons. First, the flow inside the liquid drop is at low Mach number[56] (Ma < 0.3), as an example using the speed of sound in water ($c \approx 1481$ m/s[57], Ma $= U/c \sim 10^{-3}$–10^{-4}) across our tested frequency range is well below the conventional Ma < 0.3 threshold for incompressible-flow treatment, as the relative density perturbations in a low-Mach-number flow[20,58] scale as $O(\mathrm{Ma}^2)$. Second, the liquids should be nearly incompressible materially. Comparing the capillary (Young–Laplace) pressure driving the oscillation, $\sigma/H_0 \sim 60$ Pa, using $\sigma \approx 0.072$ N/m for water[20,57,59], to water's bulk modulus, $K \approx 2.2$ GPa[57], gives an expected fractional density change of $\delta\rho/\rho \sim \Delta P/K \sim 10^{-8}$[20]. Both estimates indicate that Θ is negligible for the mechanical shape oscillation studied here, as opposed to a genuine compressional (acoustic) disturbance[58], which makes the dilatational term $(\kappa\,\Theta(\mathbf{x},t)^2)$ in Eq. (8) negligible regardless of the value of κ itself. Neglecting this term gives

$$\Phi(t) = \frac{2\mu}{V}\int_V D'_{ij}(\mathbf{x},t)\,D'_{ij}(\mathbf{x},t)\,\mathrm{d}V. \tag{10}$$

Eq. (10) remains a good approximation regardless of the true value of κ and coincides exactly with the incompressible form $\Phi = (2\mu/V)\int_V D_{ij}D_{ij}\,\mathrm{d}V$ whenever $\Theta \approx 0$.

Substituting Eq. (7) into Eq. (9) gives

$$D_{ij}(\mathbf{x},t) = \sigma_1\dot{q}_1(t)\,E_{ij}(\mathbf{x},P), \qquad E_{ij}(\mathbf{x},P=1) = \frac{1}{2}\left(\frac{\partial u_{1i}(\mathbf{x})}{\partial x_j} + \frac{\partial u_{1j}(\mathbf{x})}{\partial x_i}\right), \tag{11}$$

where E_{ij} is a purely geometric, time-independent quantity. Because the trace is a linear operation, the deviatoric part inherits the same separation of time and space,

$$D'_{ij}(\mathbf{x},t) = \sigma_1\dot{q}_1(t)\,E'_{ij}(\mathbf{x},P), \qquad E'_{ij} = E_{ij} - \frac{1}{3}\delta_{ij}\left(\nabla\cdot\mathbf{u}_1\right). \tag{12}$$

To express this in terms of $\dot{S}(t)$, we note from Eq. (6) that $\dot{S}(t) = \beta\,\mathrm{sgn}(q_1)\,\dot{q}_1(t)$, so that $\sigma_1\dot{q}_1(t) = \mathrm{sgn}(q_1)\,(\sigma_1/\beta)\,\dot{S}(t)$ and

$$D'_{ij}(\mathbf{x},t) = \underbrace{\frac{\sigma_1}{\beta}}_{C}\ \mathrm{sgn}(q_1)\,\dot{S}(t)\,E'_{ij}(\mathbf{x},P) = C\,\mathrm{sgn}(q_1)\,\dot{S}(t)\,E'_{ij}(\mathbf{x},P), \tag{13}$$

where

$$C = \frac{\sigma_1}{\beta} = \frac{\sum_{k=1}^{M}|r_k^{(0)}|}{\sum_{k=1}^{M}|u_{1k}|} \tag{14}$$

is a finite constant set by the equilibrium drop size and the dominant mode shape. The sign factor $\mathrm{sgn}(q_1)$ is immaterial for the dissipation because Φ depends on $D'_{ij}D'_{ij}$ and is therefore quadratic in $\dot{S}$. Substituting Eq. (13) into Eq. (10) gives

$$\Phi(t) = 2\mu\,C^2\,\dot{S}(t)^2\left(\frac{1}{V}\int_V E'_{ij}(\mathbf{x},P)\,E'_{ij}(\mathbf{x},P)\,\mathrm{d}V\right). \tag{15}$$

Under the single-mode assumption, the dimensionless constant ($K = C^2V^{-1}\int_V E'_{ij}(\mathbf{x},P)\,E'_{ij}(\mathbf{x},P)\,\mathrm{d}V$) depends on the dominant mode drop shape and the drop size. K is not evaluated from the silhouette, but rather empirically fitted to the data. For unsteady Stokes flow, the interior structure carries a Stokes-layer dependence, so K is generally a function of frequency and geometry rather than a universal constant. Nevertheless, our experiments suggest that its frequency dependence is weak under the conditions tested. Thus, retaining additional SVD modes replaces the single scalar dissipation coefficient K with a modal dissipation matrix. The diagonal terms describe the dissipation associated with individual modes, whereas the off-diagonal terms account for coupling between modes. Although SVD modes are orthogonal under the image-space inner product, this orthogonality does not generally require the corresponding strain-rate fields to be orthogonal under the volume integral above; therefore, the cross-mode terms need not vanish.

Eq. (14) is likewise specific to the single-mode approximation. For multiple modes, the measured sloshiness is

$$S(t) = \frac{\sum_k \left| \sum_p \sigma_p u_{pk} q_p(t) \right|}{\sum_k |r_k^{(0)}|}. \tag{16}$$

Therefore, in general, it cannot be written as a sum of independent modal sloshiness amplitudes because the absolute value is applied after the modal contributions are combined. Consequently, there is no general scalar replacement for C in Eq. (14); a multi-mode formulation must retain the individual temporal modal coordinates $q_p(t)$, together with their modal dissipation coefficients and cross-mode coupling terms. For the present study, we therefore retain the dominant-mode approximation and treat

$$\Phi(t) = 2K\mu\, \dot{S}(t)^2. \tag{17}$$

as the reduced-order representation of the full modal dissipation. This approximation is supported by the strong dominance of the first SVD mode and by the experimentally observed collapse of independently measured dissipation with $(\dot{S}^2)$, while the implications of the omitted modes are discussed in Section 4.2.

Our data suggest that the dependence of K on oscillation frequency is weak, and we therefore treat K as constant in our experiments. As such, for a Newtonian drop undergoing a dominant repeating deformation mode, the viscous dissipation rate per unit volume is proportional to the dynamic viscosity and to the square of the sloshiness rate,

$$\Phi(t) \propto \mu\, \dot{S}(t)^2 \tag{18}$$

A test of Eq. (18) requires independent quantification of viscous dissipation apart from sloshiness. We quantify the viscous dissipation rate from decay of the drop center-of-mass displacement s_{cm} upon the impulsive stop of our vibrating drop platform. Since the drop oscillates on a stationary, rigid, flat surface with a pinned contact line, and under the single-mode approximation, the translational kinetic energy and deformational (internal rotation) kinetic energy decay at the same rate[60]. Two orthogonal camera views are used to track the centroidal displacement, yielding two measurements s_1 and s_2. A representative ring-down of the drop center-of-mass is shown in **Fig. 4**a. The amplitude of the envelope formed by oscillation peaks is $A(t) = A_0 e^{-\zeta\omega_{\mathrm{n}}t}$, where A_0 is the initial amplitude, ζ is the damping ratio, $\omega_{\mathrm{n}} = \omega_{\mathrm{d}}(1-\zeta^2)^{-1}$ is the undamped natural frequency, and ω_{d} is the damped natural frequency. Damped natural frequencies and damping ratios for drops with various volumes and viscosities are shown in **Fig. 5**. Natural frequency generally decreases with increasing drop volume (**Fig. 5**a), while the damping ratio increases strongly with viscosity within our test range (**Fig. 5**b).

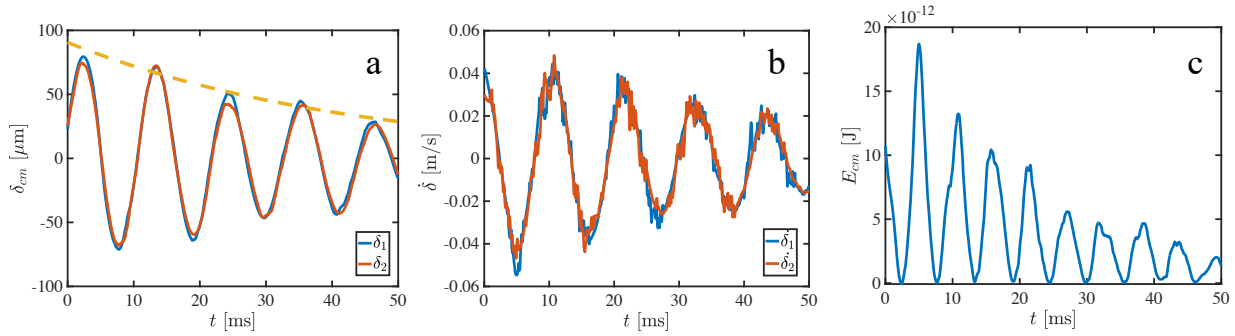


Figure 4: Kinematic response of a sessile drop following the impulsive stop of the vibrating platform. **(a)** Drop center-of-mass displacement s versus time during ring-down. Dashed curve depicts envelope formed by oscillation peaks. **(b)** Centroid velocity components obtained from two orthogonal camera views, $\dot{s}_1(t)$ and $\dot{s}_2(t)$. **(c)** Drop center-of-mass kinetic energy $E_{\mathrm{cm}}(t)$ versus time, corresponding to the results of Eq. (19).

The temporal kinetic energy of the drop during ring-down is approximated by tracking the velocity of the center-of-mass. We use the average measured from two orthogonal views,

$$E_{\mathrm{cm}}(t) \approx \frac{1}{4} m \left(\dot{s}_1(t)^2 + \dot{s}_2(t)^2 \right), \tag{19}$$

where m is the drop mass, and $\dot{s}_1(t)$ and $\dot{s}_2(t)$ are orthogonal, centroid velocity components. The net decay of the kinetic energy of the drop provides a proxy for viscous dissipation since we consider scenarios in which the contact line is pinned, and, once forcing ceases, the net loss of oscillation energy must be due to viscous dissipation. Representative plots of the centroid velocity during ring-down and the corresponding kinetic energy are shown in **Fig. 4**b,c.

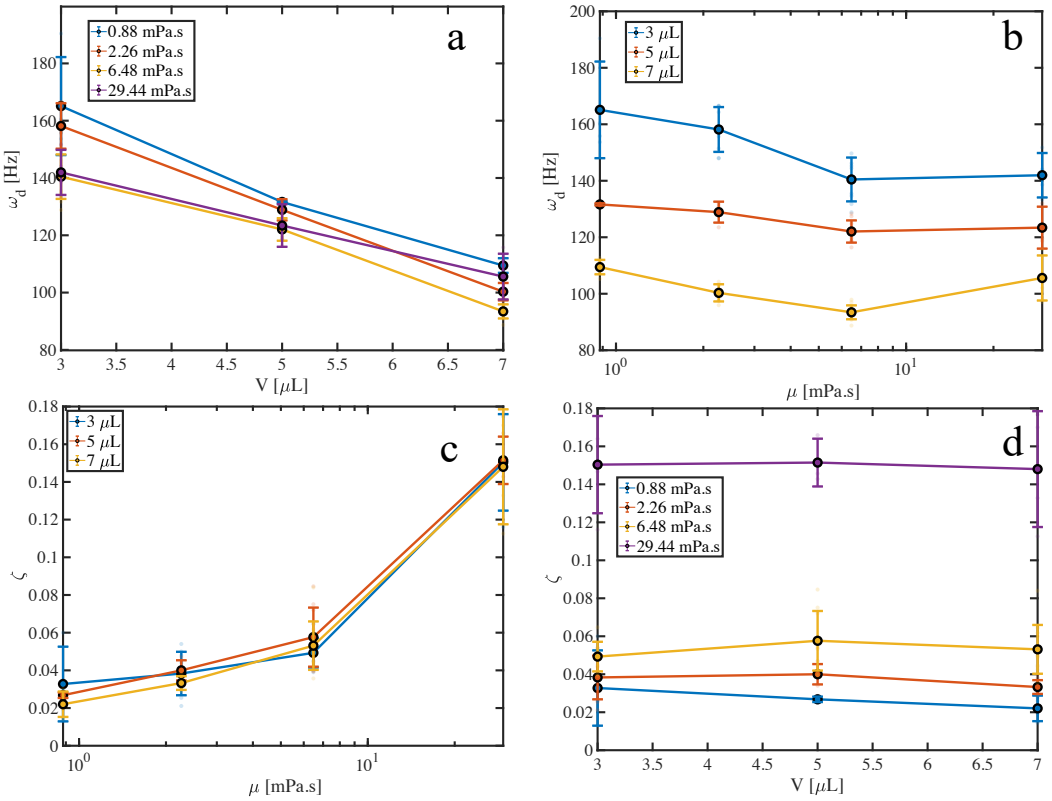


Figure 5: Measured damped natural frequency ω_d and damping ratio ζ for drops with different volumes V and viscosities μ. **(a)** ω_d versus V. **(b)** ω_d versus μ. **(c)** ζ versus μ. **(d)** ζ versus V.

Once the substrate motion ceases, viscous dissipation causes the envelope of the drop's oscillation to decay monotonically, evident in the shrinking peak-to-peak amplitude of the centroid displacement (**Fig. 4**a). The instantaneous kinetic energy, in contrast, continues to oscillate each cycle as it is reversibly exchanged with interfacial energy, falling to near zero at each turning point before rising again to a peak that is itself lower than the previous cycle (**Fig. 4**c). The experimental proxy $-\dot{E}_{cm}(t)/V$ oscillates within each cycle as kinetic energy is reversibly exchanged with interfacial energy , and only its net over a cycle reflects irreversible loss . We therefore summarize it using a time-average over the recording time, denoted $\bar{\Phi} = 1/T \int_0^T (-\dot{E}_{cm}(t)/V)dt$, which cancels the reversible contribution over the oscillation cycles. To compare experiments across different drop sizes and fluids, we form dimensionless variables,

$$X = \frac{\frac{1}{T}\int_0^T \left(\dot{S}(t)\right)^2 \, \mathrm{d}t}{\omega_d^2}, \tag{20}$$

and

$$Y = \frac{\bar{\Phi}}{\mu\omega_d^2}. \tag{21}$$

We employ ω_d to nondimensionalize Eqs. (20) and (21) because it is the dominant frequency of our freely vibrating drops. Expressing Eqs. (20) and (21) in terms of Eq. (18) we obtain,

$$Y \propto X. \tag{22}$$

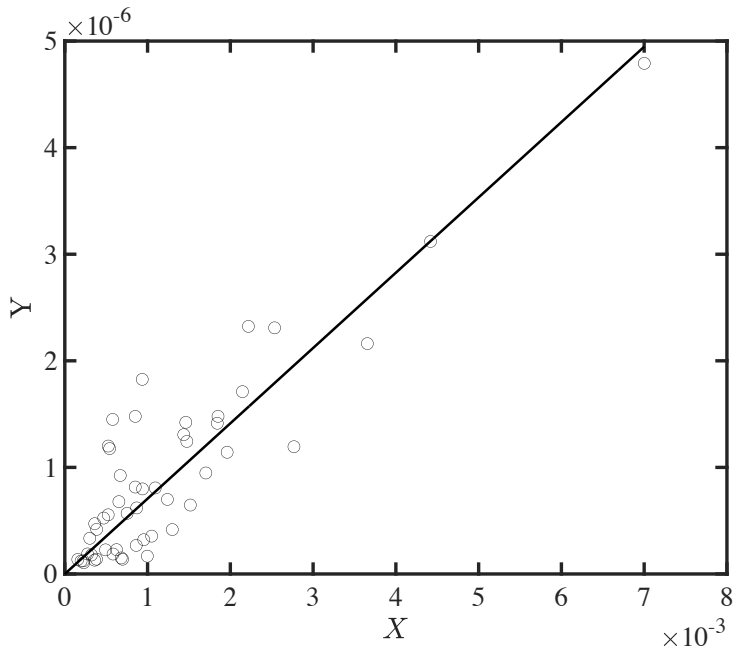


Figure 6: Normalized dissipation rate $Y = \bar{\Phi}/(\mu\omega_d^2)$ as a function of normalized sloshiness rate $X = (1/T\int_0^T(\dot{S}^2)dt)/\omega_d^2$. Best fit curve ($R^2 = 0.89$) supports theoretical prediction that viscous dissipation scales with the square of the sloshiness rate.

We plot normalized dissipation rate Y versus normalized sloshiness rate X in **Fig. 6** and show that measurements support Eq. (22) across approximately two orders of magnitude of sloshiness rate with a correlation coefficient $R^2 = 0.89$. This agreement provides an independent experimental test, as $\dot{S}$ is obtained from silhouette pixel counting, whereas $\bar{\Phi}$ is determined independently from the decay envelope of the centroid velocity. The two axes of **Fig. 6** therefore derive from separate measurements of the same experiment. The correlation confirms that Eq. (18), derived under the single-mode approximation, holds as an empirical scaling relationship across our tested range of drop volume and viscosity, and it retroactively justifies treating K as approximately constant, as if K was varied substantially with ω_d across our conditions, the collapse of Y onto a single linear trend would not be expected. This validation permits the use of $\dot{S}(t)$, a purely image-based quantity, as a proxy for viscous dissipation throughout the remainder of this work, including the energy-transmission model developed in Section 3.2. Approximately 11% of the variance in **Fig. 6** remains unexplained. This residual should not be equated directly with the $20-25\%$ of deformation variance not captured by the dominant SVD mode. The former quantifies scatter about the experimentally observed dissipation–$\dot{S}^2$ relationship, whereas the latter quantifies deformation variance represented by higher SVD modes. Since viscous dissipation depends on the squared strain-rate field rather than directly on deformation variance, the contribution of higher modes to dissipation need not scale in proportion to their SVD variance. Thus, the 75–80% variance captured by the dominant mode is consistent with, but does not quantitatively determine, the 11% residual in the dissipation correlation. Higher-mode deformation, non-axisymmetric mode mixing, residual contact-line dissipation, and image-processing uncertainty may each contribute to this remaining scatter, as discussed in Section 4.2.

3.2 Drop energy transmission in steady-state oscillation

We now consider the case where the drop is driven by a steady, vertically oscillating surface, rather than the impulsively stopped substrate and subsequent ring-down of the drop. After an initial transient, the drop reaches a periodic steady-state. At steady state, temporal averaging over any number of complete oscillation cycles gives,

$$\bar{P}_{in} = \bar{\Phi}, \tag{23}$$

where $\bar{P}_{in}$ is the time-averaged power transmitted from the oscillating surface to the drop per unit of volume. Using the dissipation scaling derived in Eq. (17), the time-averaged dissipation becomes

$$\bar{\Phi} = 2\mu K \dot{\bar{S}}^2. \tag{24}$$

We note that, for steady periodic oscillations, $\dot{\bar{S}}^2 = \mathrm{RMS}(\dot{S})^2$. As such, average power transmitted to the drop from the oscillating substrate can be written as

$$\bar{P}_{\mathrm{in}} = 2\mu K \times \mathrm{RMS}(\dot{S})^2. \tag{25}$$

Eq. (25) states that the steady-state power density transmitted from the vibrating surface to the drop can be estimated directly from the measured sloshiness dynamics, enabling the quantification of energy transmission from image-based measurements without requiring access to the internal velocity field. We model the pinned drop as a simplified point–mass system connected to a surface with amplitude $\mathcal{A}(t) = \mathcal{A}_0 \sin(\omega t)$ (**Fig. 1**) whose dynamics are well-known, where ω is the vibration frequency. The drop centroid has a displacement relative to its equilibrium position as $Z(t) = Z_0 \sin(\omega t + \phi)$, where ϕ is the phase of the centroid motion relative to the surface. In this simplified physical analogy, surface tension acts as the restoring spring force and internal viscous stresses provide damping, mirroring the reduced spring–mass–damper operator structure derived for the driven, viscous sessile drop considered in previous studies [9,38]. Rather than deriving the inertia, capillarity, and dissipation operators from first principles, we use a single empirically measured natural frequency ω_{d} and damping ratio ζ, obtained directly from free-decay data (Section 3.1).

The definition of sloshiness in the drop corresponds to $Z(t)/H_0$ in the spring–mass–damper system, where H_0 is the equilibrium height of the drop. However, there is a rheological difference between a dynamically scaled point mass and a drop, due to the absence of a velocity gradient in the former. Therefore, the proposed relation $S(t) \sim Z(t)/H_0$ requires modification to account for the non-uniformity of internal velocity across the drop. We introduce a coefficient $\Gamma(\omega)$, formally derived below, that measures how uniformly the drop's internal velocity is distributed across its height. Physically, fluid immediately adjacent to the oscillating substrate must move with it. Because the drop's contact line is pinned, its footprint diameter is fixed, which by continuity constrains the vertical velocity away from the substrate to be nearly independent of height. We refer to this height-independent value as the bulk velocity. The near-wall fluid transitions from the substrate's velocity to this bulk value over some length scale, which can be small or large relative to the drop height depending on viscosity and driving frequency. When this transition length scale is small relative to the drop height, the transition is confined to a thin region near the substrate, and most of the drop moves at the same bulk velocity, that in this limit, $\Gamma \to 0$. When the transition length scale instead approaches or exceeds the drop height, the velocity has not settled to the bulk value anywhere within the drop, and the entire profile varies continuously from substrate to free surface, and also in this limit, $\Gamma \to 1$. The quantity $1 - \Gamma(\omega)$ therefore measures the degree of internal non-uniformity, and is applied as a correction factor in Eq. (26) to account for this effect in the point-mass approximation of sloshiness. The modified sloshiness proportionality can therefore be written as

$$S(t) = C_s \left[\frac{|Z(t)|}{H_0} \left(1 - \Gamma(\omega)\right) \right]^{\alpha}, \tag{26}$$

where C_s and α are fitting parameters determined from experimental data. Given the definition of sloshiness as the relative magnitude of drop deformation, we employ the absolute values of $Z(t)$ in Eq. (26). Substituting $Z(t) = Z_0 \sin(\omega t + \phi)$ into Eq. (26) and differentiating with respect to t gives

$$\dot{S}(t) = C_s \alpha \omega \left[\frac{Z_0 \left(1 - \Gamma(\omega)\right)}{H_0} \right]^{\alpha} \mathrm{sgn}\left[\sin(\omega t + \phi)\right] \cos(\omega t + \phi) \left|\sin(\omega t + \phi)\right|^{\alpha - 1}. \tag{27}$$

$\dot{S}$ is in practice obtained as a finite difference from discrete frames acquired at 12,000 fps, and the sloshiness signal itself is derived from pixel-counting, which is inherently sampled. This finite sampling interval ensures $\dot{S}$ is bounded. The root-mean-square of $\dot{S}(t)$ is

$$\mathrm{RMS}\left(\dot{S}(t)\right)^2 = \frac{1}{T} \int_0^T \dot{S}(t)^2 \, \mathrm{d}t = C_\alpha \, \omega^2 \left[\frac{Z_0 (1 - \Gamma(\omega))}{H_0} \right]^{2\alpha}. \tag{28}$$

C_α is a fitting coefficient that absorbs α and C_s. Completing Eq. (26) requires the amplitude Z_0, which we obtain from the base-excited point-mass analogy introduced in **Sec. 3.2**. The substrate moves as $\mathcal{A}(t) = \mathcal{A}_0 \sin(\omega t)$, and the drop centroid is modeled as a damped mass at a position $z(t)$. Because sloshiness quantifies deformation, the physically relevant quantity is the centroid's motion relative to the substrate, $Z(t) = z(t) - \mathcal{X}(t)$. A drop translating rigidly with

the substrate has zero relative displacement and, correctly, zero deformation, regardless of how far the substrate itself travels. Writing the equation of motion for this relative coordinate,

$$\ddot{Z} + 2\zeta\omega_{\mathrm{d}}\dot{Z} + \omega_{\mathrm{d}}^2 Z = -\ddot{\mathcal{X}} = \omega^2 \mathcal{X}_0 \sin(\omega t), \tag{29}$$

and solving for the steady-state response amplitude gives the relative-motion transmissibility[61],

$$\frac{Z_0}{\mathcal{A}_0} = \frac{\left(\frac{\omega}{\omega_d}\right)^2}{\sqrt{\left[1 - \left(\frac{\omega}{\omega_{\mathrm{d}}}\right)^2\right]^2 + \left(2\zeta\frac{\omega}{\omega_{\mathrm{d}}}\right)^2}}. \tag{30}$$

This relative-motion transmissibility differs from the more commonly cited absolute-motion transmissibility (relating $z(t)$ directly to $\mathcal{A}(t)$), which carries an additional $\sqrt{1 + (2\zeta\omega/\omega_{\mathrm{d}})^2}$ factor in the numerator. That expression describes how much the mass moves in a fixed frame, not how much it deforms relative to its support[61], and is not the quantity relevant here. In this equation, Z_0 is assumed to oscillate at the driving substrate frequency because the centroid position is insensitive by construction to sectoral-type ($l \geq 2$) deformation[62], which justifies the harmonic assumption in Eq. (30).

To estimate $\Gamma(\omega)$, we apply a Stokes boundary-layer correction based on the classical solution for oscillatory flow above a vibrating plate. By applying our non-uniformity correction factor to a one-dimensional point-mass analogy, we neglect the full internal flow of the drop. Consider fluid velocity changes between the point of contact with the substrate and the drop bulk. In the near-wall region, the velocity difference between the substrate and bulk varies over the viscous penetration depth δ_v, whereas lateral variations occur over a characteristic length comparable to the contact radius R. Thus, the relevant gradient ratio is

$$\left|\frac{\partial w/\partial z}{\partial w/\partial x}\right| \sim \frac{w/\delta_v}{w/R} = \frac{R}{\delta_v}. \tag{31}$$

For the drops tested $3-7$ μL with equilibrium contact angles of $79° - 87°$, contact radius is $R \approx 1.2 - 1.6$ mm and drop height is $H_0 \approx 1.1 - 1.5$ mm. In the low-viscosity regime, for example $\mu = 0.88$ mPa·s, $\delta_v = 43 - 75$ μm over the $155 - 50$ Hz frequency range, giving $R/\delta_v \approx 16 - 36$. Hence, within the near-wall region, vertical velocity gradients exceed lateral gradients by more than an order of magnitude, supporting the one-dimensional approximation used here. This scaling is progressively less restrictive as δ_v approaches R or H_0. In particular, for the most viscous liquid studied ($\mu = 393.5$ mPa·s), $\delta_v \approx 0.90 - 1.58$ mm, which is comparable to the drop dimensions, and the assumption $\delta_v \ll R$, H_0 is no longer satisfied throughout the drop. We therefore interpret the one-dimensional solution as a near-substrate boundary-layer approximation rather than a description of the complete three-dimensional velocity field. The resulting Γ correction accounts for the finite penetration of the near-wall shear region into the drop. Deviations from the one-dimensional approximation near the apex and contact line are absorbed into the empirically calibrated model coefficient. Therefore, the vertical momentum balance is approximated as

$$\rho\frac{\partial w}{\partial t} = -\frac{\partial p}{\partial z} + \mu\frac{\partial^2 w}{\partial z^2}, \tag{32}$$

where $w(z,t)$ is the vertical velocity component, $p(z,t)$ is the dynamic pressure. Applying the incompressible continuity to the drop bulk yields

$$\frac{\partial u_{\mathrm{bulk}}}{\partial x} + \frac{\partial v_{\mathrm{bulk}}}{\partial y} + \frac{\partial w_{\mathrm{bulk}}}{\partial z} = 0. \tag{33}$$

Given that lateral flow is small compared to vertical flow due to the pinning of the contact diameter, we obtain

$$\frac{\partial w_{\mathrm{bulk}}}{\partial z} \approx 0. \tag{34}$$

As such, bulk vertical velocity is independent of the z-direction and can be denoted as W_{bulk}. Considering oscillatory motion, the velocity field takes the form $W(z)e^{i\omega t}$, which can be decomposed and expressed as

$$W(z) = W_{\text{bulk}} + \tilde{W}(z), \tag{35}$$

where W_{bulk} is the velocity amplitude of the bulk region and $\tilde{W}(z)$ is the difference between fluid velocity in the bulk region and near the surface. Consistent with this harmonic velocity ansatz, we similarly write the dynamic pressure as $p(z,t) = P(z)e^{i\omega t}$, with $P(z)$ its amplitude. Substituting $w(z,t) = W(z)e^{i\omega t}$ and $p(z,t) = P(z)e^{i\omega t}$ into Eq. (32) and canceling the common factor $e^{i\omega t}$ gives

$$i\omega\rho W(z) = -\frac{dP}{dz} + \mu\frac{d^2W}{dz^2}, \tag{36}$$

Following standard boundary-layer treatment, the pressure gradient dP/dz is imposed by the outer (bulk) flow and is treated as uniform across the thin near-wall region[63], so it takes the same value in both the bulk and near-wall equations that follow. Since W_{bulk} is independent of z (Eq. (34)), the viscous term in Eq. (36) vanishes in the bulk, reducing the vertical momentum balance there to

$$i\omega\rho W_{\text{bulk}} = -\frac{dP}{dz}. \tag{37}$$

This expression isolates the pressure gradient driving the bulk motion. Substituting Eq. (35) into the full near-wall form of Eq. (32) yields

$$i\omega\rho\left(W_{\text{bulk}} + \tilde{W}\right) = -\frac{dP}{dz} + \mu\frac{d^2\tilde{W}}{dz^2}. \tag{38}$$

Substituting Eq. (37) into Eq. (38) yields

$$i\omega\rho\tilde{W} = \mu\frac{d^2\tilde{W}}{dz^2}. \tag{39}$$

This is a linear, constant-coefficient ODE, with $\nu = \mu/\rho$, whose general solution is $\tilde{W}(z) = Ae^{\lambda z} + Be^{-\lambda z}$, where

$$\lambda = \sqrt{i\omega/\nu} = \frac{1+i}{\sqrt{2\nu/\omega}} = \frac{1+i}{\delta_v}, \tag{40}$$

using $\sqrt{i} = (1+i)/\sqrt{2}$, Eq. (40) gives the viscous penetration depth, or Stokes penetration depth[20] $\delta_v = \sqrt{2\nu/\omega}$. Since $\text{Re}(\lambda) > 0$, the term $Ae^{\lambda z}$ grows without bound away from the substrate. Because $\tilde{W}$ represents the velocity difference between the near-wall and bulk regions, and this difference must vanish far from the substrate, physical boundedness requires $A = 0$, leaving $\tilde{W}(z) = Be^{-\lambda z}$. The remaining constant B is fixed by the no-slip condition at the substrate ($z = 0$), where the fluid must move with the substrate velocity $W(0) = W_{\text{bulk}} + \tilde{W}(0) = W_0$, giving $B = W_0 - W_{\text{bulk}}$ and therefore

$$\tilde{W}(z) = (W_0 - W_{\text{bulk}})\, e^{-\lambda z}. \tag{41}$$

The full velocity solution is therefore

$$w(z,t) = \text{Re}\left\{\left[W_{\text{bulk}} + (W_0 - W_{\text{bulk}})\, e^{-\lambda z}\right] e^{i\omega t}\right\}, \tag{42}$$

Eq. (42) indicates the velocity gradually changes from the wall velocity to the bulk velocity over the length scale δ_v. We now formalize Γ using the velocity decomposition of Eq. (35). Because $\tilde{W}(z)$ is, by construction, the entire height-dependent part of the velocity field, its magnitude at each height directly measures how far the fluid remains from the single shared bulk value, so that $\tilde{W}(0) = W_0 - W_{\text{bulk}}$ is maximal at the substrate and decays with height over the length scale δ_v. Whether this deviation is confined to a thin fraction of the drop or persists across its entire height depends on δ_v relative to H_0, so we define Γ as the average of the normalized deviation $\tilde{W}(z)/(W_0 - W_{\text{bulk}})$ over the drop's own finite extent, $z \in [0, H_0]$. When $\delta_v \ll H_0$, the near-wall deviation occupies only a small fraction of the averaging window and is diluted toward zero, and when $\delta_v \gg H_0$, the deviation remains close to its maximum across the entire window. Evaluating this average analytically gives

$$\Gamma = \frac{1}{H_0\,(W_0 - W_{\text{bulk}})}\int_0^{H_0} \text{Re}\big[\tilde{W}(z)\big]\; dz = \frac{\delta_v}{2H_0}\left[1 - e^{-H_0/\delta_v}\left(\cos\frac{H_0}{\delta_v} - \sin\frac{H_0}{\delta_v}\right)\right]. \tag{43}$$

Plugging Eq. (43) into Eq. (26), the sloshiness is then expressed as

$$S(t) = \left[\frac{|Z(t)|}{H_0}\left(1 - \frac{\delta_v}{2H_0}\left[1 - e^{-H_0/\delta_v}\left(\cos\frac{H_0}{\delta_v} - \sin\frac{H_0}{\delta_v}\right)\right]\right)\right]^{\alpha}. \tag{44}$$

Substituting Eqs. (44), (30), and (28) into Eq. (25), we obtain

$$\bar{P}_{\text{in}} = 2KC_{\alpha}\mu\,\frac{(1-\Gamma(\omega))^{2\alpha}}{H_0^{2\alpha}}\omega^2\mathcal{X}_0^{2\alpha}\left[\frac{\left(\frac{\omega}{\omega_{\text{n}}}\right)^2}{\sqrt{\left[1-\left(\frac{\omega}{\omega_{\text{n}}}\right)^2\right]^2 + \left(2\zeta\,\frac{\omega}{\omega_{\text{n}}}\right)^2}}\right]^{2\alpha}. \tag{45}$$

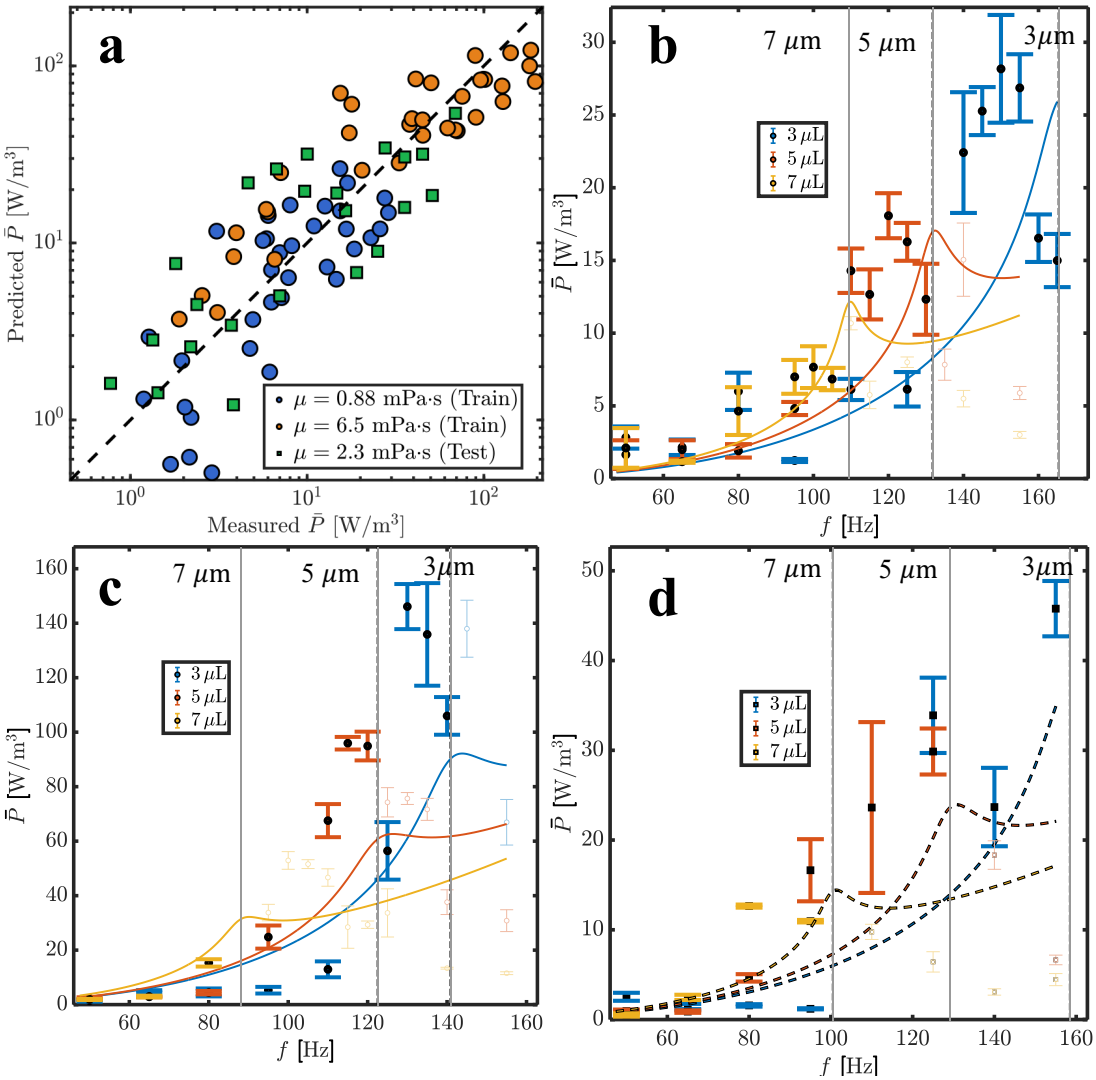


Figure 7: **(a)** Predicted versus measured transmitted power trained on $\mu = 0.88$ and 6.5 mPa·s and tested on the unseen fluid $\mu = 2.3$ mPa·s, across the full frequency range. The dashed line represents the ideal prediction (Measured $\bar{P}$ = Predicted $\bar{P}$). Predicted $\bar{P}$ is calculated by Eq. (45) (solid/dashed curves) re-fitted on the full range of frequency for the two fitting fluids: **(b)** $\mu = 0.88$ mPa·s, **(c)** $\mu = 6.5$ mPa·s, and **(d)** the unseen test fluid $\mu = 2.3$ mPa·s. (b-d) Solid markers denote pre-resonance data ($f \leq f_n$) and faded hollow markers denote post-resonance data ($f > f_n$), which lie outside the validity range of the model. Vertical dashed lines represent the natural frequency of drops.

Equation (45) establishes the functional form of the transmitted power, relating $\bar{P}_{\text{in}}$ to driving frequency, substrate amplitude, liquid viscosity, drop geometry, and the drop's own measured natural frequency and damping ratio. The exponent α and C_α, however, are not determined by the derivation itself and must be estimated from experimental data before Eq. (45) can be used for prediction. We therefore test whether the model, once calibrated using a subset of our measurements, can predict the transmitted power for drop conditions not included in the calibration data, as shown in **Fig. 7**. We divide the experimental data into two groups, a fitting set and a test set, to empirically fit and evaluate the utility of Eq. (45) for predicting the rate of energy transmission into a liquid drop. The determination of fitting parameters for Eq. (45) using experimental measurements for $\mu = 0.88$ and 6.5 mPa·s across the full frequency range yields $\alpha = 0.159$. A result of $\alpha \neq 1$ precludes $S \sim |Z|/H_0$, which may reflect contributions from higher-mode deformation and the restricted centroid motion imposed by the pinned contact line. We test the model for $\mu = 2.3$ mPa·s. For each driven-oscillation trial, we obtain an experimental estimate of $\bar{P}_{\text{in}}$ by extracting $\dot{S}(t)$ directly from the drop silhouette (Eq. (1)), computing $\text{RMS}(\dot{S})^2$ over the trial, and evaluating Eq. (25) using the fluid's known viscosity μ. This estimate is compared against the model prediction of Eq. (45), plotted in **Fig. 7**a. Because both quantities depend on the same fitted K, this comparison tests whether the base-excitation and boundary-layer corrections (Eq. (30), Eq. (43)) correctly predict the sloshiness response, given K as established independently from free decay, rather than testing K itself. The corresponding R^2 values for the fitting and test sets are poor at 0.7 and 0.53, respectively. To probe further, prediction curves for the transmitted power are plotted alongside experimental measurements for the full frequency range in **Fig. 7**b-d. We observe that Eq. (45) fails to capture the reduction in transmitted energy observed at frequencies above resonance. We consider several candidate explanations for this reduction, which carry differing degrees of quantitative support.

The leading candidate is that the drop lacks sufficient time to restore its equilibrium shape before the substrate completes each oscillation cycle, progressively suppressing its sloshiness. This hypothesis predicts that suppression should begin once the viscocapillary relaxation time[64], $\mu H_0/\sigma$, becomes comparable to the substrate oscillation period, $1/f$. For our most viscous fluid at our highest driving frequency, these timescales are indeed comparable ($\mu H_0/\sigma \sim 7$ ms versus $1/f \approx 6.5$ ms at 155 Hz), consistent with this mechanism, whereas for our lower-viscosity fluids, $\mu H_0/\sigma$ remains one to three orders of magnitude smaller than $1/f$ throughout our tested range, so this mechanism does not, by itself, account for the same qualitative suppression observed at lower viscosities.

We hypothesize that this remaining discrepancy instead reflects a limitation of the centroid-based prediction, rather than a failure of the underlying transmission model. Centroid position is insensitive by construction to non-axisymmetric ($l \geq 2$) surface deformation[36]. The transition from harmonic, axisymmetric response to subharmonic, non-axisymmetric response has been linked to driving acceleration[62,65] exceeding a threshold on the order of $1g$. At fixed substrate displacement amplitude, acceleration scales as $(2\pi f)^2$ and so increases sharply with frequency in our own experiments, plausibly bringing higher-frequency trials into this regime. If such a transition occurs, the centroid-based prediction of $\dot{S}$ could be suppressed without a corresponding suppression of the true, silhouette-derived sloshiness rate.

Regardless of which mechanism is responsible, this post-resonance behavior is not captured by Eq. (45), and the physically valid range of the model is therefore restricted to frequencies at or below the resonance frequency of the drop.

Restricting fitting data to the pre-resonance regime ($f \leq f_n$) and re-fitting yields $\alpha = 0.171$. Despite the inherent variability in experimental measurements, R^2 values for the fitting and test sets improve substantially to 0.8 and 0.77, respectively, confirming that Eq. (45) provides a physically consistent and quantitatively reliable description of the energy transmission in the pre-resonance regime. As established by the results shown in **Fig. 8**, energy from the oscillating substrate to the drop at the natural frequency of the drop decreases per unit volume as drop volume increases.

We validate this observation by using a simple free-vibration ring-down experiment, in which a drop is deposited on the tip of a plucked vibrating cantilever, as described in Section 2. A representative plot of the displacement Δ of the plucked cantilever tip in a ring-down experiment is shown by **Fig. 9**. Increasing the number of drops while keeping the total liquid volume constant at $V = 18$ μL increases the decay rate by increasing the total contact area and δ_v/H_0, as shown in **Fig. 10**a. Indeed, smaller drops have a larger dissipative capacity per unit volume (**Fig. 8**b-d). In addition, according to $\bar{P}_{\text{in}} \propto \mu \times \text{RMS}(\dot{S})^2$ (Eq. (25)), increasing viscosity increases the transmitted energy up to a threshold, beyond which the reduction in drop deformation at high viscosity decreases the transmitted energy. This result is also observed by obtaining the decay rate of the cantilever after testing drops with different viscosity but with the same volume $V = 10$ μL. As viscosity increases from 0.88 mPa·s [1W0G] to 29.44 mPa·s [1W3G], transmitted energy increases, while, on the other hand, it decreases from $\mu = 29.44$ mPa·s to $\mu = 393.5$ mPa·s for glycerol, as shown in **Fig. 10**b.

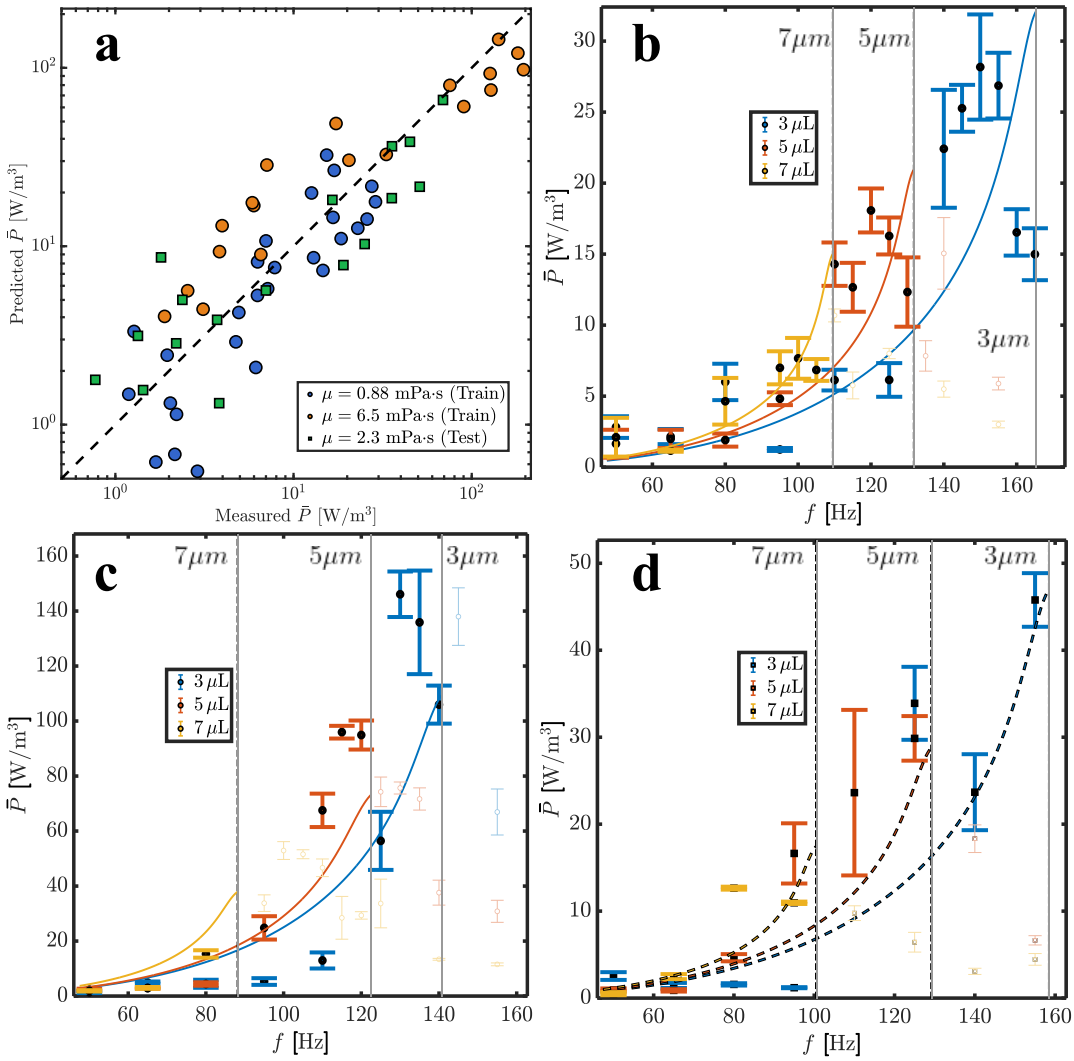


Figure 8: Predicted versus measured transmitted power trained on $\mu = 0.88$ and 6.5 mPa·s and tested on the unseen fluid $\mu = 2.3$ mPa·s, across the pre-resonance frequency range. The dashed line represents the ideal prediction. Transmitted power P_{meas} as a function of excitation frequency against the model prediction of Eq. (45) (solid/dashed curves) re-fitted on the pre-resonance data Panels for **(b, c)** the two fitting fluids $\mu = 0.88$ mPa·s and $\mu = 6.5$ mPa·s, and **(d)** the unseen test fluid $\mu = 2.3$ mPa·s. (c-d) Solid markers denote pre-resonance data ($f \leq f_n$) and faded hollow markers denote post-resonance data ($f > f_n$), which lie outside the validity range of the model. Vertical dashed lines represent the natural frequency of drops.

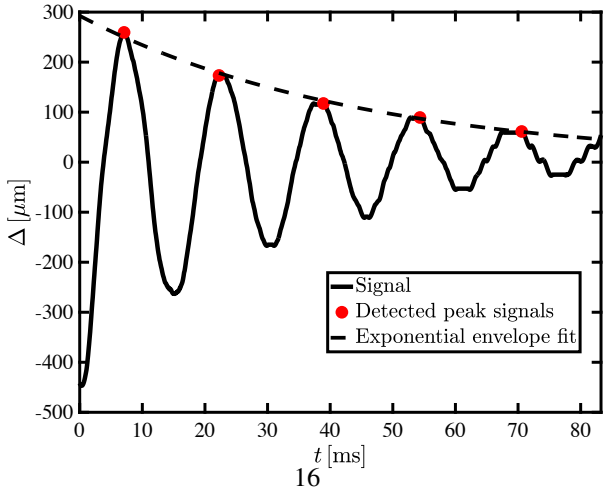


Figure 9: Representative free-vibration ring-down response of the plucked cantilever with a 10 μL glycerol drop [0W1G] deposited at the tip. The cantilever displacement decays exponentially after release, and the fitted envelope gives a damped natural frequency of $f_d = 63.15$ Hz, damping ratio of $\zeta = 0.056$, and decay rate of $b = 22.2$ s^{-1}.

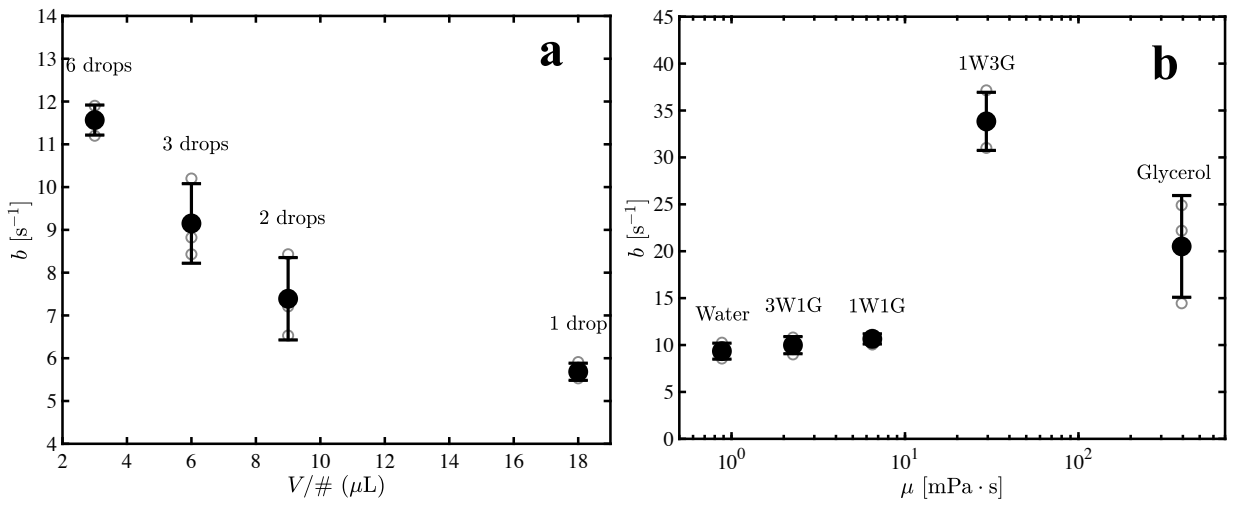


Figure 10: Decay rate of the cantilever free vibration. **(a)** Decay rate b vs individual drop volume, keeping total volume constant at 18 μL. The decay rate increases as the individual volume of 1W0G drops decreases. **(b)** Decay rate vs viscosity for 10 μL drops. The decay rate initially increases with increasing viscosity but decreases at very high viscosity as drop deformation becomes suppressed. Error bars represent $\pm$ one standard deviation.

4 Discussion

In this study, we connect viscous dissipation and energy transmission to image-based drop silhouette deformation (Eq. (18)), which eliminates the need for time-resolved measurements or computations of the drop internal velocity field for cases where it is challenging to access the internal flow field measurement, which is true for many applications. Examples include opaque fluids such as crude oils and liquid metals[66,67], or drops under extreme conditions, such as high temperatures[68,69] or cryogenic temperatures[70,71], in which introducing and maintaining suitable tracers is difficult. In some cases, it is unallowable to add impurities to a sample, such as in nuclear-grade liquids[72] and biofluids . We acknowledge that many of the aforementioned example liquids can exhibit some degree of non-Newtonian behavior. The applicability of our method to non-Newtonian liquids is an area for future work. Even for Newtonian, transparent drops, the constant change in drop curvature produces optical distortion that requires post-processing correction to achieve accurate velocity field measurements[73,74]. A further practical advantage is that surface tension does not appear explicitly in our framework. Surface tension governs the natural frequency and damping ratio of the drop, but because ω_n and ζ are measured directly from free-decay ring-down data rather than predicted from liquid properties, our method sidesteps the need for independent surface tension measurements. Avoiding the need for a prescribed surface tension value is particularly advantageous for contaminated or multicomponent liquids, for which surface tension may be difficult to measure or may vary over time, such as during evaporation or chemical reactions. The trade-off is that the model cannot predict energy transmission for a new liquid without first performing a ring-down experiment to obtain ω_n and ζ.

4.1 Physical interpretation of the energy transmission model

The Stokes penetration depth relative to the drop height is the dimensionless parameter that controls the volumetric energy transmission efficiency, consistent with classical results for oscillating viscous drops; dissipation is concentrated in a boundary layer near the interface and can dominate the total dissipation even when bulk viscosity is weak[75,76]. When δ_v/H_0 is very small, a strong velocity gradient exists, but it is confined to a thin boundary layer close to the wall. The bulk above the boundary layer contributes to inertia and reversible energy recovery. Still, the bulk does not participate in meaningful dissipation, so the spatially localized shear layer hinders the substrate's ability to perform irreversible work on the whole of the drop. The non-dissipating bulk thus dilutes the transmission power per unit volume. When $\delta_v/H_0 \to 1$, the viscous layer spans much of the drop, homogenizing the velocity field and, as a result, the viscous dissipation begins to vanish due to the diminishment of the velocity gradient. Therefore, there is a non-

monotonic power transfer dependence on δ_v/H_0 that indicates that the maximum transmission efficiency occurs when the shear layer is thick enough to engage a considerable portion of the drop but thin enough to maintain shear in the velocity field.

Our interpretation is validated by an independent cantilever experiment shown as **Fig. 10**. For a low-viscosity fluid such as water ($\delta_v \approx 0.05$mm) that sits deep in the $\delta_v << H_0$ regime across the range of drop volumes, reducing the size of the drop increases δ_v/H_0 toward a peak dissipative capacity per unit volume. Further decreasing drop size lowers dissipation capacity as smaller drops lose the ability to slosh[77]. Thus, small drops behave similarly to larger, more viscous drops. This non-monotonic behavior, previously observed empirically for drops damping a vibrating cantilever[17], is confirmed here in **Fig. 10**b, where the peak in energy transfer/dissipation from the cantilever to the drop occurs at an intermediate value of δ_v/H_0. Eq. (18) identifies the underlying mechanism as the competing roles of μ in amplifying dissipative capacity while suppressing the sloshiness rate itself.

In addition to drop size and viscosity, vibration frequency ω governs δ_v/H_0. In the pre-resonance regime, increasing ω decreases the viscous penetration depth δ_v while increasing the sloshiness rate (Eq. (28)). The former is weaker than the latter as evidenced by the $2\alpha < 1$ exponent in Eq. (45). In the post-resonance regime, a sudden decrease in transmission energy $\bar{P}_{\text{in}}$ is observed because the drop is unable to follow the translation of the substrate, as stated by Eq. (30) and shown in by **Fig. 7**b-d. However, the current model does not predict the suppression of the sloshiness rate (Eq. (28)), which constitutes a failure when the substrate vibrates faster than resonance.

4.2 Limitations and future work

The dissipation scaling $\Phi \propto \mu \dot{S}^2$ (Eq. (18)) and the transmission model (Eq. (25)) rest on assumptions whose validity defines the current scope of our model and whose relaxation points toward natural extensions for future work. The single-mode approximation (Eq. (3)) requires that the first singular value σ_1 accounts for the majority of the deformation energy. In our experiments, the first mode captures approximately 75-80 % of the total variance ($\sigma_1^2/\sum_i \sigma_i^2$). The dominance of the primary mode is expected for drops driven well below the onset frequency of higher-order shape modes. Near mode transitions or at high forcing amplitudes, higher modes may contribute more significantly, and the single-mode truncation will be less accurate. Mode mixing between a harmonic zonal component and a subharmonic non-axisymmetric one has been reported in the large majority (> 90%) of observations in comparable pinned, driven sessile-drop systems[38], raising the possibility that some portion of the ∼20% of variance not captured by σ_1 reflects such coexisting content. Theory attributes the harmonic zonal response to a low-amplitude meniscus wave with no true excitation threshold, distinct from non-axisymmetric modes, which are genuine parametric instabilities governed by a threshold computable via Floquet analysis[65]. Viscous Floquet-based parametric instability theory has been established for planar interfaces[78] and free spherical drops[79], but no corresponding theory exists yet for a sessile drop with a pinned contact line, particularly across the viscosity range studied here. Extending our approach to retain multiple SVD modes is straightforward in principle; the dissipation would be expressed as a sum over modal contributions and would broaden the range of forcing conditions to which the method applies.

The dissipation integral (Eq. (8)) requires velocity gradients throughout the drop volume, yet sloshiness is computed from the two-dimensional silhouette. The implicit assumption is that the surface deformation encodes the internal flow structure. For the dominant-mode oscillations considered here, the measured boundary deformation provides sufficient information to construct a reduced-order estimate of the volumetric strain-rate field. This assumption is justified when the drop deforms in an axisymmetric mode on a horizontal, flat substrate with uniform wettability[80,81], because axisymmetry ensures that two orthogonal silhouettes fully determine the three-dimensional free-surface shape, and for low-order modes the internal flow is kinematically slaved to the surface motion. A sessile drop on a vertically vibrating flat substrate remains axisymmetric provided the driving acceleration stays below the parametric (Faraday) threshold for all non-axisymmetric modes[65,82,83]. These assumptions fail for drops on inclined or heterogeneous substrates, or for higher-order modes with internal recirculation not visible in the silhouette.

The correlation between the sloshiness-rate-based dissipation estimate and the independently measured dissipation rate yields $R^2 = 0.89$ (**Fig. 6**), leaving approximately 11 % of the variance unexplained. Three factors likely contribute to the less-than-perfect fit. First, contact-line dissipation is not captured by the bulk viscous scaling $\Phi \propto \mu \dot{S}^2$. Although the rough substrate suppresses gross contact-line motion, residual microscopic slip may still dissipate energy. Incorporating a contact-line dissipation term, such as the model already developed for driven sessile drops by Bostwick & Steen[9], is likely to improve the correlation and allow its extension to drops with gross contact-line motion. Second, higher-mode content is not captured by the single-mode truncation and introduces deformation energy that is invisible to the model, an issue that could be addressed by the multi-mode extension described above. On a related note, K may

exhibit systematic variation due to modal frequency content and geometry. Third, image-processing noise propagates into both $\dot{S}$ and $\dot{E}_{\mathrm{cm}}$, adding scatter to both axes of the correlation. The relative contributions of these three sources are not resolved by the present study.

The one-dimensional Stokes correction also has a geometric limitation. The derivation assumes that the near-substrate velocity variation occurs over the viscous penetration depth δ_v, while lateral variations occur over the larger contact-radius scale R. For the present low-viscosity cases, $R/\delta_v \gtrsim O(10)$, supporting the neglect of lateral gradients within the near-wall region. However, as δ_v/H_0 approaches unity, the distinction between a thin boundary layer and the remainder of the drop becomes less pronounced, and the one-dimensional approximation becomes increasingly restrictive. Moreover, near the apex and contact-line regions, the local interface curvature introduces lateral length scales that are not represented by the planar Stokes solution. Eq. (43) should therefore be interpreted as a leading-order correction for the near-substrate velocity non-uniformity rather than an exact representation of the three-dimensional internal flow. A fully resolved treatment would require solving the coupled three-dimensional flow in the actual sessile-drop geometry, including the curved free surface and pinned contact line.

The energy transmission model (Eq. (45)) is validated only in the pre-resonance regime. Above the natural frequency, the substrate oscillation period becomes shorter than the drop shape relaxation timescale, a time not quantified analytically, and the drop can no longer respond periodically to the forcing. The resulting suppression of sloshiness is not captured by the harmonic single-degree-of-freedom analogy underlying Eq. (28).

The fitted exponent α is specific to the mapping between centroid motion and the present silhouette-based definition of sloshiness. The value of α is consistent across the different drop sizes and viscosities tested on the same surface, whereas its dependence on surface properties is not resolved by the present study.

5 Conclusion

We establish a physical link between the visible deformation of an oscillating sessile drop and its internal viscous dissipation. By decomposing the drop surface deformation into data-driven modes via singular value decomposition and assuming a single dominant mode, we show that the viscous dissipation rate per unit volume is proportional to the product of the dynamic viscosity and the square of the sloshiness rate, $\Phi \propto \mu\, \dot{S}^2$. This relationship enables estimation of viscous dissipation directly from drop silhouette image sequences without requiring measurements or computations of the internal velocity field.

For steady-state harmonic oscillations, the time-averaged power transmitted from a vibrating substrate is balanced by viscous dissipation, allowing the transmitted power to be expressed in terms of sloshiness dynamics. Combining this energy balance with a base-excited spring–mass–damper analogy and a Stokes boundary-layer correction for the internal velocity non-uniformity, we develop a semi-empirical model (Eq. (45)) that predicts how transmitted power varies with excitation frequency, substrate amplitude, liquid viscosity, and drop size. The model is fitted using data from two liquids and successfully predicts the transmitted power for a withheld fluid with $R^2 = 0.77$ in the pre-resonance regime ($f \leq f_n$). Above the natural frequency, where the substrate oscillation period becomes shorter than the drop shape relaxation timescale, the drop can no longer respond periodically to the forcing. The resulting suppression of sloshiness is not captured by the current model, restricting its validity to the pre-resonance regime.

Independent cantilever ring-down experiments corroborate two predictions of our model. First, for a fixed total liquid volume, distributing the liquid among a larger number of smaller drops increases the cantilever decay rate, confirming that smaller drops dissipate more energy per unit volume. Smaller drops have a larger ratio of viscous penetration depth to drop height, which engages a greater fraction of the liquid volume in the near-wall shear layer. Second, the cantilever decay rate varies non-monotonically with liquid viscosity. Decay rate initially increases as viscosity enhances the capacity for irreversible work, then decreases at higher viscosities as the drop becomes too solid-like to slosh appreciably. The presence of a maximally dissipative viscosity is a direct consequence of the dissipation scaling $\Phi \propto \mu\, \dot{S}^2$, in which viscosity amplifies dissipation per unit deformation rate while simultaneously suppressing the deformation rate itself.

Taken together, these results demonstrate that the dynamic silhouette of a sessile drop contains sufficient information to characterize both viscous dissipation and energy transmission without optical or computational access to the internal flow. The framework requires only high-speed video from two orthogonal views, making it practical for parametric studies within the range of Newtonian liquids, drop sizes and forcing conditions examined here.

Acknowledgements

The authors thank Dr. Emazuddin Alif for his methodological contributions. The authors acknowledge the use of Claude Opus 5 for ensuring that theoretical model assumptions and execution in Sections 3.1 & 3.2 are error-free.

Declaration of Interests. The authors report no conflict of interest.

References

[1] Renardy, Y. Y. & Cristini, V., 2001 Effect of inertia on drop breakup under shear. *Physics of Fluids* **13**, 7–13. (doi:10.1063/1.1331321).

[2] Sheth, K. S. & Pozrikidis, C., 1995 Effects of inertia on the deformation of liquid drops in simple shear flow. *Computers & Fluids* **24**, 101–119. (doi:10.1016/0045-7930(94)00025-5).

[3] Finn, R., 1999 Capillary surface interfaces. *Notices of the American Mathematical Society* **46**, 770–781.

[4] Zhang, X., 1999 Dynamics of drop formation in viscous flows. *Chemical Engineering Science* **54**, 1759–1774. (doi:10.1016/S0009-2509(99)00027-5).

[5] Chen, L. & Bonaccurso, E., 2014 Effects of surface wettability and liquid viscosity on the dynamic wetting of individual drops. *Physical Review E* **90**, 022401. (doi:10.1103/PhysRevE.90.022401).

[6] Lyubimov, D. V., Lyubimova, T. P. & Shklyaev, S. V., 2006 Behavior of a drop on an oscillating solid plate. *Physics of Fluids* **18**, 012101. (doi:10.1063/1.2137358).

[7] Wilkes, E. D. & Basaran, O. A., 1997 Forced oscillations of pendant (sessile) drops. *Physics of Fluids* **9**, 1512–1528. (doi:10.1063/1.869276).

[8] Deepu, P., Chowdhuri, S. & Basu, S., 2014 Oscillation dynamics of sessile droplets subjected to substrate vibration. *Chemical Engineering Science* **118**, 9–19. (doi:10.1016/j.ces.2014.07.028).

[9] Bostwick, J. B. & Steen, P. H., 2016 Response of driven sessile drops with contact-line dissipation. *Soft Matter* **12**, 8919–8926. (doi:10.1039/C6SM01928E).

[10] Sharp, J. S., 2012 Resonant properties of sessile droplets; contact angle dependence of the resonant frequency and width in glycerol/water mixtures. *Soft Matter* **8**, 399–407. (doi:10.1039/C1SM06916K).

[11] Rostami, P., Castrejon-Pita, A. A. & Auernhammer, G. K., 2025 Rheological insights from the oscillation dynamics of viscoelastic sessile drops. *arXiv preprint arXiv:2509.12006* (doi:10.48550/arXiv.2509.12006).

[12] Smuda, M., Kummer, F., Oberlack, M., Zrnic, D. & Brenn, G., 2024 From weakly to strongly nonlinear viscous drop shape oscillations: An analytical and numerical study. *Physical Review Fluids* **9**, 063601. (doi:10.1103/PhysRevFluids.9.063601).

[13] Li, J., Zhao, C. & Wang, C., 2023 Experimental study on the dynamics of droplet impacting on solid surface. *Microfluidics and Nanofluidics* **27**, 69. (doi:10.1007/s10404-023-02680-1).

[14] Biroun, M. H., Taghipour, J., Ikhlaq, M., Howarth, J., Mazzei, L. & Fu, Y.-Q., 2025 Energy dissipation mechanisms during droplet impact on superhydrophobic surfaces. *Physics of Fluids* **37**, 052107. (doi:10.1063/5.0258079).

[15] Li, X.-H., Zhang, X.-X. & Chen, M., 2015 Estimation of viscous dissipation in nanodroplet impact and spreading. *Physics of Fluids* **27**, 052007. (doi:10.1063/1.4921141).

[16] Bansal, S. & Sen, P., 2017 Axisymmetric and nonaxisymmetric oscillations of sessile compound droplets in an open digital microfluidic platform. *Langmuir* **33**, 11047–11058. (doi:10.1021/acs.langmuir.7b02042).

[17] Alam, M. E. & Dickerson, A. K., 2021 Sessile liquid drops damp vibrating structures. *Physics of Fluids* **33**, 062113. (doi:10.1063/5.0055382).

[18] Sanyal, A. & Basu, S., 2018 Evaporation excites temporal sequence of resonant modes in a sessile droplet perturbed at constant frequency: Insights into the universal dynamics of mode transitions. *Chemical Engineering Science* **176**, 294–305. (doi:10.1016/j.ces.2017.10.053).

[19] Xu, F., Zhang, L. & Xia, K.-Q., 2024 Experimental measurement of spatio-temporally resolved energy dissipation rate in turbulent rayleigh–bénard convection. *Journal of Fluid Mechanics* **984**, A8. (doi:https://doi.org/10.1017/jfm.2024.164).

[20] Landau, L. D. & Lifshitz, E. M., 1987 *Fluid Mechanics*, volume 6 of *Course of Theoretical Physics*. Pergamon Press, 2nd edition.

[21] Poulain, S. & Carlson, A., 2023 Sliding, vibrating and swinging droplets on an oscillating fibre. *Journal of Fluid Mechanics* **967**, A24. (doi:10.1017/jfm.2023.462).

[22] Wang, G., Yang, F., Wu, K., Ma, Y., Peng, C., Liu, T. & Wang, L.-P., 2021 Estimation of the dissipation rate of turbulent kinetic energy: A review. *Chemical Engineering Science* **229**, 116133. (doi:10.1016/j.ces.2020.116133).

[23] Tanaka, T. & Eaton, J. K., 2010 Sub-kolmogorov resolution particle image velocimetry measurements of particle-laden forced turbulence. *Journal of Fluid Mechanics* **643**, 177–206. (doi:10.1017/S0022112009992023).

[24] Stanislas, M., Okamoto, K., Kähler, C. J., Westerweel, J. & Scarano, F., 2008 Main results of the third international piv challenge. *Experiments in Fluids* **45**, 27–71. (doi:10.1007/s00348-008-0462-z).

[25] Keane, R. D. & Adrian, R. J., 1990 Optimization of particle image velocimeters. Part I: Double pulsed systems. *Measurement Science and Technology* **1**, 1202–1215. (doi:10.1088/0957-0233/1/11/013).

[26] Meinhart, C. D. & Wereley, S. T., 2003 The theory of diffraction-limited resolution in microparticle image velocimetry. *Measurement Science and Technology* **14**, 1047–1053. (doi:10.1088/0957-0233/14/7/320).

[27] Meinhart, C. D., Wereley, S. T. & Santiago, J. G., 2000 A PIV algorithm for estimating time-averaged velocity fields. *Journal of Fluids Engineering* **122**, 285–289. (doi:10.1115/1.483256).

[28] Santiago, J. G., Wereley, S. T., Meinhart, C. D., Beebe, D. J. & Adrian, R. J., 1998 A particle image velocimetry system for microfluidics. *Experiments in Fluids* **25**, 316–319. (doi:10.1007/s003480050235).

[29] Sharma, N., Bachalo, W. D. & Agarwal, A. K., 2020 Spray droplet size distribution and droplet velocity measurements in a firing optical engine. *Physics of Fluids* **32**, 023304. (doi:10.1063/1.5126498).

[30] Burgmann, S., Dues, M., Barwari, B., Steinbock, J., Büttner, L., Czarske, J. & Janoske, U., 2021 Flow measurements in the wake of an adhering and oscillating droplet using laser-doppler velocity profile sensor. *Experiments in Fluids* **62**, 47. (doi:10.1007/s00348-021-03148-0).

[31] Sciacchitano, A., 2019 Uncertainty quantification in particle image velocimetry. *Measurement Science and Technology* **30**, 092001. (doi:10.1088/1361-6501/ab1db8).

[32] Tang, X., Saha, A., Sun, C. & Law, C. K., 2019 Spreading and oscillation dynamics of drop impacting liquid film. *Journal of Fluid Mechanics* **881**, 859–871. (doi:10.1017/jfm.2019.771).

[33] Lee, J. B., Derome, D., Dolatabadi, A. & Carmeliet, J., 2016 Energy budget of liquid drop impact at maximum spreading: Numerical simulations and experiments. *Langmuir* **32**, 1279–1288. (doi:10.1021/acs.langmuir.5b03848).

[34] Yasuri, A. K., 2025 Energy dissipation mechanisms in droplet dynamics: implications for wetting phenomena. *Microfluidics and Nanofluidics* **29**, 71. (doi:10.1007/s10404-025-02846-z).

[35] Rayleigh, L., 1879 On the capillary phenomena of jets. *Proceedings of the Royal Society of London* **29**, 71–97. (doi:10.1098/rspl.1879.0015).

[36] Bostwick, J. & Steen, P., 2014 Dynamics of sessile drops. part 1. inviscid theory. *Journal of Fluid Mechanics* **760**, 5–38. (doi:10.1017/jfm.2014.582).

[37] Bostwick, J. & Steen, P., 2015 Stability of constrained capillary surfaces. *Annual Review of Fluid Mechanics* **47**, 539–568. (doi:10.1146/annurev-fluid-010814-013626).

[38] Chang, C.-T., Bostwick, J., Daniel, S. & Steen, P., 2015 Dynamics of sessile drops. part 2. experiment. *Journal of Fluid Mechanics* **768**, 442–467. (doi:10.1017/jfm.2015.99).

[39] Joseph, D. D. & Wang, J., 2004 The dissipation approximation and viscous potential flow. *Journal of Fluid Mechanics* **505**, 365–377. (doi:10.1017/S0022112004008602).

[40] Watson, D. A., Souchik, C. J., Weinberg, M. P., Bom, J. M. & Dickerson, A. K., 2020 Making a splash with fabrics in hydrophilic sphere entry. *Journal of Fluids and Structures* **94**, 102907. ISSN 0889-9746. (doi:10.1016/j.jfluidstructs.2020.102907).

[41] Savitzky, A. & Golay, M. J. E., 1964 Smoothing and differentiation of data by simplified least squares procedures. *Analytical Chemistry* **36**, 1627–1639. (doi:10.1021/ac60214a047).

[42] Schafer, R. W., 2011 What is a savitzky-golay filter? *IEEE Signal Processing Magazine* **28**, 111–117. (doi:10.1109/MSP.2011.941097).

[43] Watson, D. A., Bom, J. M., Weinberg, M. P., Souchik, C. J. & Dickerson, A. K., 2021 Water entry dynamics of spheres with heterogeneous wetting properties. *Physical Review Fluids* **6**, 044003. (doi:10.1103/PhysRevFluids.6.044003).

[44] Watson, D. A., Anzola, S., Zeas, F. A., Smith, K. B. & Cruz, A. A., 2024 Compound cavity formation and splash crown suppression by water entry through proximally adjacent polystyrene beads. *Physics of Fluids* **36**, 092124. ISSN 1070-6631. (doi:10.1063/5.0226769).

[45] Watson, D. A., Joseph, Z. C., Vidana-Fuentes, D. A., Anzola, S. & Zeas, F. A., 2025 Water entry dynamics of hydrophobic spheres bounded by semi-infinite cylindrical pipes. *Physics of Fluids* **37**, 112115. ISSN 1070-6631. (doi:10.1063/5.0300541).

[46] Schmid, M., Rath, D. & Diebold, U., 2022 Why and how Savitzky–Golay filters should be replaced. *ACS Measurement Science Au* (doi:10.1021/acsmeasuresciau.1c00054).

[47] Taira, K., Brunton, S. L., Dawson, S. T., Rowley, C. W., Colonius, T., McKeon, B. J., Schmidt, O. T., Gordeyev, S., Theofilis, V. & Ukeiley, L. S., 2017 Modal analysis of fluid flows: An overview. *AIAA journal* **55**, 4013–4041. (doi:10.2514/1.J056060).

[48] Giorgi, M.-L., Duval, H. & Balabane, M., 2021 The proper orthogonal decomposition: A powerful tool for studying drop oscillations. *Review of Scientific Instruments* **92**, 113903. (doi:10.1063/5.0056004).

[49] Abdi, H., 2007 Singular value decomposition (svd) and generalized singular value decomposition (gsvd). In *Encyclopedia of Measurement and Statistics* (ed. N. Salkind), pp. 907–912. Thousand Oaks, CA: Sage.

[50] García-Magariño, A., Sor, S. & Velazquez, A., 2016 Data reduction method for droplet deformation experiments based on high order singular value decomposition. *Experimental Thermal and Fluid Science* **79**, 13–24. (doi:10.1016/j.expthermflusci.2016.06.017).

[51] Eckart, C. & Young, G., 1936 The approximation of one matrix by another of lower rank. *Psychometrika* **1**, 211–218. (doi:10.1007/BF02288367).

[52] Honda, K., Fujiwara, K., Hasegawa, K., Kaneko, A. & Abe, Y., 2023 Coalescence and mixing dynamics of droplets in acoustic levitation by selective colour imaging and measurement. *Scientific Reports* **13**, 19590. (doi:10.1038/s41598-023-46008-z).

[53] Lamb, H., 1881 On the oscillations of a viscous spheroid. *Proceedings of the London Mathematical Society* **1**, 51–70. (doi:10.1112/plms/s1-13.1.51).

[54] Batchelor, G. K., 1967 *An Introduction to Fluid Dynamics*. Cambridge University Press.

[55] Aris, R., 1962 *Vectors, Tensors, and the Basic Equations of Fluid Mechanics*. Prentice-Hall.

[56] Anderson, J. D., 2017 *Fundamentals of Aerodynamics*. McGraw-Hill Education, 6 edition.

[57] Haynes, W. M. (ed.), 2016 *CRC Handbook of Chemistry and Physics*. CRC Press, 97 edition.

[58] Papalexandris, M. V., 2020 On the applicability of Stokes' hypothesis to low-Mach-number flows. *Continuum Mechanics and Thermodynamics* **32**, 1245–1249. (doi:10.1007/s00161-019-00785-z).

[59] Young, T., 1805 An essay on the cohesion of fluids. *Philosophical Transactions of the Royal Society of London* **95**, 65–87. (doi:10.1098/rstl.1805.0005).

[60] Sakakeeny, J. & Ling, Y., 2021 Numerical study of natural oscillations of supported drops with free and pinned contact lines. *Physics of Fluids* **33**, 062109. (doi:10.1063/5.0049328).

[61] Hundal, M. S., 1979 Response of a base excited system with coulomb and viscous friction. *Journal of Sound and Vibration* **64**, 371–378. (doi:10.1016/0022-460X(79)90583-6).

[62] Chang, C.-T., Bostwick, J. B., Steen, P. H. & Daniel, S., 2013 Substrate constraint modifies the rayleigh spectrum of vibrating sessile drops. *Physical Review E—Statistical, Nonlinear, and Soft Matter Physics* **88**, 023015. (doi: 10.1103/PhysRevE.88.023015).

[63] Schlichting, H. & Gersten, K., 2017 *Boundary-Layer Theory*. Berlin, Heidelberg: Springer, 9 edition. (doi: 10.1007/978-3-662-52919-5).

[64] Reboucas, R. B., Nikolova, N. N. & Sharma, V., 2025 Modeling drop deformations and rheology of dilute to dense emulsions. *Current Opinion in Colloid & Interface Science* **77**, 101904. (doi:10.1016/j.cocis.2025.101904).

[65] Ding, D., Sayyari, M. J. & Bostwick, J. B., 2024 Parametric oscillations of the sessile drop. *Journal of Fluid Mechanics* **995**, A3. (doi:10.1017/jfm.2024.632).

[66] Poelma, C., 2020 Measurement in opaque flows: a review of measurement techniques for dispersed multiphase flows. *Acta Mechanica* **231**, 2089–2111. (doi:10.1007/s00707-020-02683-x).

[67] Hyers, R. W., 2005 Fluid flow effects in levitated droplets. *Measurement Science and Technology* **16**, 394–401. (doi:10.1088/0957-0233/16/2/010).

[68] Shang, W., Chen, J., Okosun, T., Zhou, C. Q., Entwistle, J., Rodgers, B., Morey, J. & Leontaras, K., 2023 Real-time non-invasive velocity field measurement of molten iron jet discharged from blast furnace. *JOM* **75**, 2430–2440. (doi:10.1007/s11837-023-05860-0).

[69] Fang, C. & Liu, H., 2018 Particle image velocimetry for combustion measurements: Applications and developments. *Chinese Journal of Aeronautics* **31**, 1407–1427. (doi:10.1016/j.cja.2018.01.023).

[70] Bret, C., Chartier, J., Diribarne, P., Duplat, J. & Rousset, B., 2023 Controlled spherical deuterium droplets as lagrangian tracers for cryogenic turbulence experiments. *Review of Scientific Instruments* **94**, 105114. (doi: 10.1063/5.0167132).

[71] Karlsson, L., Lycksam, H., Ljung, A.-L., Gren, P. & Lundström, T. S., 2019 Experimental study of the internal flow in freezing water droplets on a cold surface. *Experiments in Fluids* **60**, 182. (doi:10.1007/s00348-019-2823-1).

[72] Ueki, Y., Noguchi, Y., Yagi, J., Tanaka, T., Yokomine, T., Hirabayashi, M., Ara, K., Kunugi, T. & Sagara, A., 2017 Ultrasonic doppler velocimetry experiment of lead-lithium flow with oroshhi-2 loop. *Fusion Science and Technology* **72**, 530–536. (doi:10.1080/15361055.2017.1330636).

[73] Gatete, E., Shen, B. & Kaneko, A., 2024 Improvement of the accuracy of piv measurement of flow field in a levitated droplet. *Mechanical Engineering Journal* **11**, 23–00315. (doi:10.1299/mej.23-00315).

[74] Saha, A., Basu, S. & Kumar, R., 2012 Particle image velocimetry and infrared thermography in a levitated droplet with nanosilica suspensions. *Experiments in Fluids* **52**, 795–807. (doi:10.1007/s00348-011-1114-2).

[75] Miller, C. & Scriven, L., 1968 The oscillations of a fluid droplet immersed in another fluid. *Journal of Fluid Mechanics* **32**, 417–435. (doi:10.1017/S0022112068000832).

[76] Prosperetti, A., 1980 Normal-mode analysis for the oscillations of a viscous liquid drop in an immiscible liquid. *Journal de Mécanique* **19**, 149–182.

[77] Kadivar, E., 2018 Modeling droplet deformation through converging–diverging microchannels at low reynolds number. *Acta Mechanica* **229**, 4239–4250. (doi:10.1007/s00707-018-2225-0).

[78] Kumar, K. & Tuckerman, L. S., 1994 Parametric instability of the interface between two fluids. *Journal of Fluid Mechanics* **279**, 49–68. (doi:10.1017/S0022112094003812).

[79] Ebo-Adou, A. & Tuckerman, L. S., 2016 Faraday instability on a sphere: Floquet analysis. *Journal of Fluid Mechanics* **805**, 591–610. (doi:10.1017/jfm.2016.542).

[80] Argatov, I. & Kocherbitov, V., 2025 Moderately low-bond-number axisymmetric drop shape analysis and tensiometry for sessile drops. *Discover Applied Sciences* **7**, 1042. (doi:10.1007/s42452-025-07677-9).

[81] Hajirahimi, M., Mokhtari, F. & Fatollahi, A. H., 2015 Exact identities for sessile drops. *Applied Mathematics and Mechanics* **36**, 293–302. (doi:10.1007/s10483-015-1916-6).

[82] Vukasinovic, B., Smith, M. K. & Glezer, A., 2007 Dynamics of a sessile drop in forced vibration. *Journal of Fluid Mechanics* **587**, 395–423. (doi:10.1017/S0022112007007379).

[83] Noblin, X., Buguin, A. & Brochard-Wyart, F., 2009 Vibrations of sessile drops. *The European Physical Journal Special Topics* **166**, 7–10. (doi:10.1140/epjst/e2009-00869-y).